



# ALMA Reveals Thermal and Nonthermal Desorption of Methanol Ice in the HD 100546 Protoplanetary Disk

Lucy Evans<sup>1</sup> , Alice S. Booth<sup>2</sup> , Catherine Walsh<sup>1</sup> , John D. Ilee<sup>1</sup> , Luke Keyte<sup>3</sup> , Charles J. Law<sup>4,10</sup> ,  
Margot Leemker<sup>5</sup> , Shota Notsu<sup>6,7</sup> , Karin Öberg<sup>2</sup> , Milou Temmink<sup>8</sup> , and Nienke van der Marel<sup>9</sup>

<sup>1</sup> School of Physics and Astronomy, University of Leeds, LS2 9JT, UK; [l.e.evans@leeds.ac.uk](mailto:l.e.evans@leeds.ac.uk), [c.walsh1@leeds.ac.uk](mailto:c.walsh1@leeds.ac.uk)

<sup>2</sup> Center for Astrophysics | Harvard & Smithsonian, 60 Garden Street, Cambridge, MA 02138, USA

<sup>3</sup> Astronomy Unit, School of Physics and Astronomy, Queen Mary University of London, London E1 4NS, UK

<sup>4</sup> Department of Astronomy, University of Virginia, Charlottesville, VA 22904, USA

<sup>5</sup> Dipartimento di Fisica, Università degli Studi di Milano, Via Celoria 16, 20133 Milano, Italy

<sup>6</sup> Department of Earth and Planetary Science, Graduate School of Science, The University of Tokyo, 7-3-1 Hongo, Bunkyo-ku, Tokyo 113-0033, Japan

<sup>7</sup> Star and Planet Formation Laboratory, RIKEN Cluster for Pioneering Research, 2-1 Hirosawa, Wako, Saitama 351-0198, Japan

<sup>8</sup> Leiden Observatory, Leiden University, PO Box 9513, 2300 RA Leiden, The Netherlands

<sup>9</sup> Leiden Observatory, Leiden University, 2300 RA Leiden, The Netherlands

Received 2024 September 27; revised 2025 January 20; accepted 2025 February 3; published 2025 March 19

## Abstract

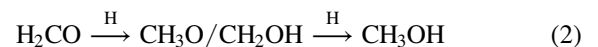
Methanol (CH<sub>3</sub>OH) and formaldehyde (H<sub>2</sub>CO) are chemically coupled organic molecules proposed to act as an intermediate step between simple molecules and more complex prebiotic compounds. Their abundance distributions across disks regulate the prebiotic potential of material at different disk radii. We present observations of multiple methanol and formaldehyde transitions toward the Herbig Ae disk HD 100546 obtained with the Atacama Large Millimeter/submillimeter Array, building upon the previous serendipitous detection of methanol in this source. We find that methanol has a higher rotational temperature ( $T_{\text{rot}}$ ) than formaldehyde toward both the centrally concentrated emission component in the inner disk (0–110 au) and a radially separate dust ring farther out in the disk (180–260 au).  $T_{\text{rot}}$  decreases for methanol and formaldehyde from the inner ( $152^{+35}_{-27}$  K and  $76^{+9}_{-8}$  K) to the outer disk ( $52^{+8}_{-6}$  K and  $31^{+2}_{-2}$  K), suggesting that we are tracing two different chemical environments.  $T_{\text{rot}}$  for both species in the inner disk is consistent with thermal desorption as the origin, while the outer disk reservoir is driven by nonthermal desorption. The CH<sub>3</sub>OH/H<sub>2</sub>CO column density ratio decreases from  $14.6^{+5.2}_{-4.6}$  in the inner disk to  $1.3^{+0.3}_{-0.2}$  in the outer disk, consistent with modeling predictions. The CH<sub>3</sub>OH/H<sub>2</sub>CO column density ratio for the inner disk is consistent with the median value in the range of column density ratios compiled from solar system comets, which would have formed at a similar distance. This supports the notion that interstellar ice is inherited and preserved by protoplanetary disks around solar-mass and intermediate-mass stars as we are seeing “fresh” ice sublimation, as well as providing more evidence for the presence of prebiotic precursor molecules in planet-forming regions.

*Unified Astronomy Thesaurus concepts:* Astrochemistry (75); Protoplanetary disks (1300); Complex organic molecules (2256); Herbig Ae/Be stars (723)

## 1. Introduction

Complex organic molecules (COMs) are defined as carbon-containing molecules with at least six atoms (E. Herbst & E. F. van Dishoeck 2009). As such, these molecules are seen as a bridge between simple molecules and more complex, prebiotic molecules that are vital for the development of life as we know it (e.g., C. Meinert et al. 2016). This is particularly relevant for the astrochemical study of star formation; many COMs have been detected toward objects at various stages of this process (e.g., E. Herbst & E. F. van Dishoeck 2009; J. K. Jørgensen et al. 2020; S. Scibelli & Y. Shirley 2020; C. Ceccarelli et al. 2023). In addition to these observations, laboratory experiments have revealed the icy origin of many COM species. The simplest COM, methanol (CH<sub>3</sub>OH), is known to form in star-forming molecular clouds when dust

grains are coated with ice (e.g., K. Hiraoka et al. 1994). When CO is frozen out onto the dust grains (typically at temperatures  $\lesssim 20$  K), it undergoes hydrogenation (shown in Equations (1) and (2)), forming formaldehyde (H<sub>2</sub>CO) in an intermediate reaction before continuing to form CH<sub>3</sub>OH (K. Hiraoka et al. 1994; N. Watanabe & A. Kouchi 2002; G. W. Fuchs et al. 2009).



Hydrogen abstraction reactions are also important for controlling the rate of H<sub>2</sub>CO and CH<sub>3</sub>OH ice formation (e.g., K. J. Chuang et al. 2016). A combination of hydrogenation and abstraction reactions can also lead to increased chemical complexity in the ice with only CO and H as the primary ingredients (e.g., G. Fedoseev et al. 2017) and without the need for energetic processing (e.g., K. I. Öberg et al. 2009; Y. J. Chen et al. 2013). For example, methyl formate is a more complex COM that can form via hydrogenation (K. J. Chuang et al. 2017; M. A. J. Simons et al. 2020). It is now known that chemical complexity can already build in

<sup>10</sup> NASA Hubble Fellowship Program Sagan Fellow.



interstellar ices in advance of the formation of stars and their surrounding planetary systems (see M. K. McClure et al. 2023; W. R. M. Rocha et al. 2024; and Y. Chen et al. 2024, for recent JWST results), although it remains an open question how much of this complexity is inherited and retained in the protoplanetary disk.

Evidence that planet formation is already likely underway at the protoplanetary disk (Class II) stage (e.g., ALMA Partnership et al. 2015) has provided even stronger motivation for the detection of COMs in these objects (see also N. F. W. Ligterink et al. 2024). Despite clear progress in detecting and characterizing the complex inventory toward less-evolved objects, it remains challenging to do so for planet-forming disks around young stars because their small angular size (typically less than a few arcseconds for the nearest star-forming regions) means that the ice sublimation zone is only a few percent of an arcsecond and thus it is difficult to resolve. However, with the recent advent of facilities with sufficiently high spatial and spectral resolution, most notably the Atacama Large Millimeter/submillimeter Array (ALMA), the characterization of the COM inventory in protoplanetary disks is now possible. The simplest COM, CH<sub>3</sub>OH, was first detected in the gas phase with ALMA toward the disk surrounding the nearby T Tauri star, TW Hya (C. Walsh et al. 2016). Despite the confirmation of the presence of CH<sub>3</sub>OH in a protoplanetary disk, subsequent observations failed to detect CH<sub>3</sub>OH in targeted studies of the disks surrounding MWC 480 and LkCa15 (R. A. Loomis et al. 2020; Y. Yamato et al. 2024), as well as HD 163296 (M. T. Carney et al. 2019), although dimethyl ether (CH<sub>3</sub>OCH<sub>3</sub>) has been detected in MWC 480 (Y. Yamato et al. 2024). Gas-phase H<sub>2</sub>CO, on the other hand, is (almost) ubiquitously observed toward both T Tauri and Herbig disks (e.g., A. Dutrey et al. 1997; W. F. Thi et al. 2004; K. I. Öberg et al. 2011; S. Guilloteau et al. 2013; A. Garufi et al. 2021; V. V. Guzmán et al. 2021; L. Rampinelli et al. 2024), with tentatively lower column densities measured toward the latter (J. Pegues et al. 2020). This is due to H<sub>2</sub>CO also having efficient gas-phase formation pathways, primarily the neutral–neutral reaction involving CH<sub>3</sub> and O (see Equation (3); C. Fockenberg & J. M. Preses 2002; D. Semenov & D. Wiebe 2011; R. A. Loomis et al. 2015), which are not affected by dust temperature and thus proceed regardless of whether or not CO is frozen out.



With Herbig stars having typical luminosities up to 4 orders of magnitude higher than T Tauri stars (C. Wichittanakom et al. 2020), the temperature of the disk surrounding these stars was considered too warm for the in situ formation of CH<sub>3</sub>OH ice because of the inability of CO ice to freeze out in the warm ( $\gtrsim 20$  K) midplanes of Herbig disks.

Given the proposed difficulty for in situ CH<sub>3</sub>OH ice formation in Herbig disks, the detection of gas-phase CH<sub>3</sub>OH in the protoplanetary disk surrounding the Herbig Ae star, HD 100546, was unexpected and indicates inheritance of the CH<sub>3</sub>OH ice reservoir from an earlier evolutionary stage (A. S. Booth et al. 2021). Moreover, two distinct emission components were detected, one being centrally concentrated with the other coincident with the previously tentatively detected dust ring at approximately 220 au. This gives rise to the possibility that two distinct desorption mechanisms are at

play in this disk, a consequence of the radial temperature gradient.

It is now known that disks around Herbig stars offer a unique insight into the composition of the ice reservoir. Gas-phase CH<sub>3</sub>OH has since been successfully detected toward HD 169142 and IRS 48. Similar to that found for HD 100546, it is thought that CH<sub>3</sub>OH (along with SO) is tracing oxygen-rich gas in these disks arising due to sublimation of the ice reservoir (A. S. Booth et al. 2021, 2023b; N. van der Marel et al. 2021). As well as HD 100546, the ices in the disks surrounding IRS 48 (N. van der Marel et al. 2021) and HD 169142 (A. S. Booth et al. 2023b) show evidence for inheritance, meaning that the ices formed prior to the current evolutionary stage. As a result of this earlier formation, the ices have undergone radial transport toward the dust trap location, where they are desorbed due to the warm nature of the dust traps in these particular disks. In other disks that have dust traps (regardless of whether they are T Tauri or Herbig) but where CH<sub>3</sub>OH remains undetected, it is suggested that this is due to the dust trap being colder; therefore, the desorption of CH<sub>3</sub>OH and other organics does not take place (see also M. Temmink et al. 2023; N. van der Marel 2023).

A more complete chemical inventory of both HD 100546 and IRS 48 has since been reported (A. S. Booth et al. 2024a, 2024b). In these works, 19 molecules have been detected toward HD 100546 and 16 toward IRS 48, including several higher-complexity COMs: CH<sub>3</sub>OCHO toward both disks and CH<sub>3</sub>OCH<sub>3</sub> and c-H<sub>2</sub>COCH<sub>2</sub> toward IRS 48 (see also N. G. C. Brunken et al. 2022; M. Leemker et al. 2023). However, these works do not determine the rotational temperature of CH<sub>3</sub>OH nor its predecessor, H<sub>2</sub>CO, toward HD 100546. The particular desorption mechanisms at play and their potential connection to an inherited origin of CH<sub>3</sub>OH in this source, in which two separate emission components have been clearly identified, have not yet been investigated. The rotational temperature of CH<sub>3</sub>OH is important to constrain in these two emission components as it may reflect the particular desorption mechanism(s) at play across different disk radii.

In this work, we present a detailed rotational diagram analysis of multiple molecular lines of H<sub>2</sub>CO and CH<sub>3</sub>OH detected toward the disk around HD 100546, observed during ALMA Cycles 7 and 8, with comparisons included between our results for HD 100546 and other objects across the various stages of the star formation process. CH<sub>3</sub>OH can only form efficiently on the grain surface and is subsequently desorbed into the gas phase; however, as previously mentioned, H<sub>2</sub>CO, an intermediary of CH<sub>3</sub>OH (refer to Equations (1) and (2)), also has efficient gas-phase formation mechanisms (C. Fockenberg & J. M. Preses 2002). H<sub>2</sub>CO is therefore an important inclusion as complementary observations allow a tighter constraint on the formation and/or destruction mechanisms at play in this source. Previous research has shown that lower CH<sub>3</sub>OH/H<sub>2</sub>CO ratios may be associated with chemical processing of accreting material as it is delivered to disks (L. Podio et al. 2020), can be a tracer of nonthermally desorbed material (M. L. R. van’t Hoff et al. 2020), as well as being able to provide an indication of efficient gas-phase formation of H<sub>2</sub>CO in the outer disk (e.g., R. A. Loomis et al. 2015; M. T. Carney et al. 2017; J. Terwisscha van Scheltinga et al. 2021; M. Temmink et al. 2023; C. Hernández-Vera et al. 2024a).

The paper is structured as follows. We describe the source (HD 100546) and the Cycle 7 and 8 ALMA observations in

Section 2 and the emission morphology of lines detected in these data in Section 3. We explain the methodology used in the rotational diagram analysis in Section 4 and present the results in Section 5, which are subsequently discussed and compared with modeling predictions in Section 6. Finally, we state our conclusions in Section 7.

## 2. Observations

### 2.1. The Disk Around HD 100546

HD 100546 (R.A. (J2000) =  $11^{\text{h}}33^{\text{m}}25^{\text{s}}.3$ , decl. (J2000) =  $-70^{\circ}11'41''.2$ ) is a nearby ( $110 \pm 1$  pc) Herbig Ae star of intermediate age ( $4.8^{+1.8}_{-0.2}$  Myr), with a mass of  $2.18^{+0.02}_{-0.17} M_{\odot}$  and a stellar effective temperature of 10,000 K, that is surrounded by a warm, gas-rich disk (J. R. Fairlamb et al. 2015; C. Wichitatanakom et al. 2020). The position angle and inclination of the disk are  $146^{\circ}$  and  $44^{\circ}$ , respectively (C. Walsh et al. 2014). Previous continuum observations detected two dust rings centered at approximately 20–40 au and 180–220 au separated by a wide dust gap (J. E. Pineda et al. 2019; D. Fedele et al. 2021), supporting the evidence for two possible giant planets embedded in the disk at approximately 10 au and 60 au (S. P. Quanz et al. 2013; S. D. Brittain et al. 2014; C. Walsh et al. 2014; P. Pinilla et al. 2015). The warm, thermally heated edge of the inner dust cavity is proposed to be the origin of compact SO, H<sub>2</sub>CO, CH<sub>3</sub>OH, and CH<sub>3</sub>OCHO emission observed with ALMA (A. S. Booth et al. 2018; A. S. Booth et al. 2021; A. S. Booth et al. 2023a).

The proximity of HD 100546 (see, e.g., L. Wölfer et al. 2024; refer also to L. Lindegren et al. 2016) has facilitated many dedicated studies, leading to the detection of multiple simple species, including SO, O, OH, C<sup>+</sup>, C, H<sub>2</sub>O, HCO<sup>+</sup>, CS, as well as multiple isotopologues of CO (D. Fedele et al. 2013; C. M. Wright et al. 2015; M. Kama et al. 2016; A. S. Booth et al. 2018; J. M. Miley et al. 2019; L. M. Pirovano et al. 2022; L. Keyte et al. 2023). This has allowed for some constraints on the disk structure and global C/O ratio; M. Kama et al. (2016) found this to be similar to solar, meaning that the disk gas is only moderately depleted in heavy elements such as C and O. Recent thermochemical modeling supports evidence for radial C/O variations across the disk shaped by the sculpted dust rings. A value for C/O of 0.8 inward of the dust rings rising to 1.2 beyond the rings better reproduces the trends in the observations (M. Leemker et al. 2024). A more recent chemical inventory reported by A. S. Booth et al. (2024a) revealed that the disk has significant molecular substructure, with rings of HCN, CN, C<sub>2</sub>H, CS, H<sub>2</sub>CS, H<sub>2</sub>CO, as well as CH<sub>3</sub>OH peaking in emission just beyond the location of the two dust rings, with oxygen-bearing species peaking both within the inner cavity and at or beyond the outer dust ring.

In summary, HD 100546 is a good target for this study as it is a nearby, well-studied disk with multiple simple organic and COM detections enabling the detailed excitation analysis of CH<sub>3</sub>OH and H<sub>2</sub>CO.

### 2.2. ALMA Observations

We use ALMA observations obtained during Cycle 8 targeting multiple lines of CH<sub>3</sub>OH in Band 7 with baselines ranging from 15–3000 m (2021.1.00738.S with A. S. Booth as PI). The imaging of these data is already described in A. S. Booth et al. (2024a), therefore we limit the description here to necessary details only. All lines were imaged using the

`tclean` task provided by the Common Astronomy Software Application (CASA),<sup>11</sup> version 5.6. We used Briggs weighting (D. S. Briggs 1995) and a multiscale deconvolver with scale sizes of 0, 5, 10, and 20 and applied a uv taper of 0.4 while cleaning down to a threshold of  $3\sigma$ , where  $\sigma$  was taken as the rms measured using CASA in emission-free areas. We applied a Keplerian mask using a Python script (first published in R. Teague 2020) during imaging, which had a radial extent of 260 au (the radial extent of the H<sub>2</sub>CO emission) and a line width set to  $200 \text{ m s}^{-1}$  at  $1''$  varying radially with an exponent of  $-0.5$ . We assumed a position angle of  $146^{\circ}$ , a disk inclination of  $44^{\circ}$  (C. Walsh et al. 2014), as well as a distance of 110 pc (C. Wichitatanakom et al. 2020).

The data were imaged using a Briggs robust parameter of 2.0 for the weaker lines to boost the signal-to-noise ratio (S/N) in the channel maps as measured using the rms value calculated from the emission-free channels of each spectral window (spw) as given by CASA. The H<sub>2</sub>CO line detected in the Cycle 8 data was strong enough to permit imaging with a robust parameter of 0.5 in order to improve spatial resolution. The resulting channel maps have a nominal beam size of  $0''.4 \times 0''.3$ , equivalent to a physical scale of 33–44 au, with a native spectral resolution of  $0.9 \text{ km s}^{-1}$ .

We detect 10 well-separated lines of CH<sub>3</sub>OH at an S/N of at least 3 (according to peak intensity in the channel maps) in this data set, as well as one transition of o-H<sub>2</sub>CO. Table 1 lists the detected lines used in this analysis, their spectroscopic data as listed in the Cologne Database for Molecular Spectroscopy (CDMS)<sup>12</sup>, along with the imaging parameters for each spectral cube. For CH<sub>3</sub>OH, the spectroscopic data in CDMS are from L.-H. Xu et al. (2008), whereas those for H<sub>2</sub>CO are from H. S. P. Müller & F. Lewen (2017). Additional CH<sub>3</sub>OH lines were detected in the data set; however, many of these, particularly around 338 GHz, are affected by blending, either with other CH<sub>3</sub>OH lines or with lines from other species; hence, we use only the lines with profiles that are clearly separated from other lines for our rotational diagram analysis. The upper energies ( $E_u$ ) of our selected lines of CH<sub>3</sub>OH span from 16–260 K, enabling the construction of a rotational diagram to determine the rotational temperature of gas-phase methanol.

We supplement our Cycle 8 data with ALMA Cycle 7 observations of o-H<sub>2</sub>CO and p-H<sub>2</sub>CO toward HD 100546 with baselines ranging from 15–2517 m (program 2019.1.00193.S with A. S. Booth as PI). These data are also described in A. S. Booth et al. (2021) and A. S. Booth et al. (2023a). The data were imaged in the same manner as described above; the resulting channel maps have a nominal beam size of  $0''.3 \times 0''.2$ , which is equivalent to a physical scale of 22–33 au, with a spectral resolution of  $0.25 \text{ km s}^{-1}$ . To better match the image resolution of the Cycle 8 data, we convolve the Cycle 7 channel maps using `imsmooth` with a beam of  $0''.4$ . The JvM correction (S. Jorsater & G. A. van Moorsel 1995) was applied to all images produced from the Cycle 7 data; epsilon was calculated as 0.3. (see I. Czekala et al. 2021, for further information). No JvM correction was applied to the images produced from the Cycle 8 data because a single configuration only was used for these data.

<sup>11</sup> <https://casa.nrao.edu/>; (CASA Team et al. 2022)

<sup>12</sup> <https://cdms.astro.uni-koeln.de/cdms/portal/>; H. S. P. Müller et al. (2001), H. S. Müller et al. (2005), and C. P. Endres et al. (2016)



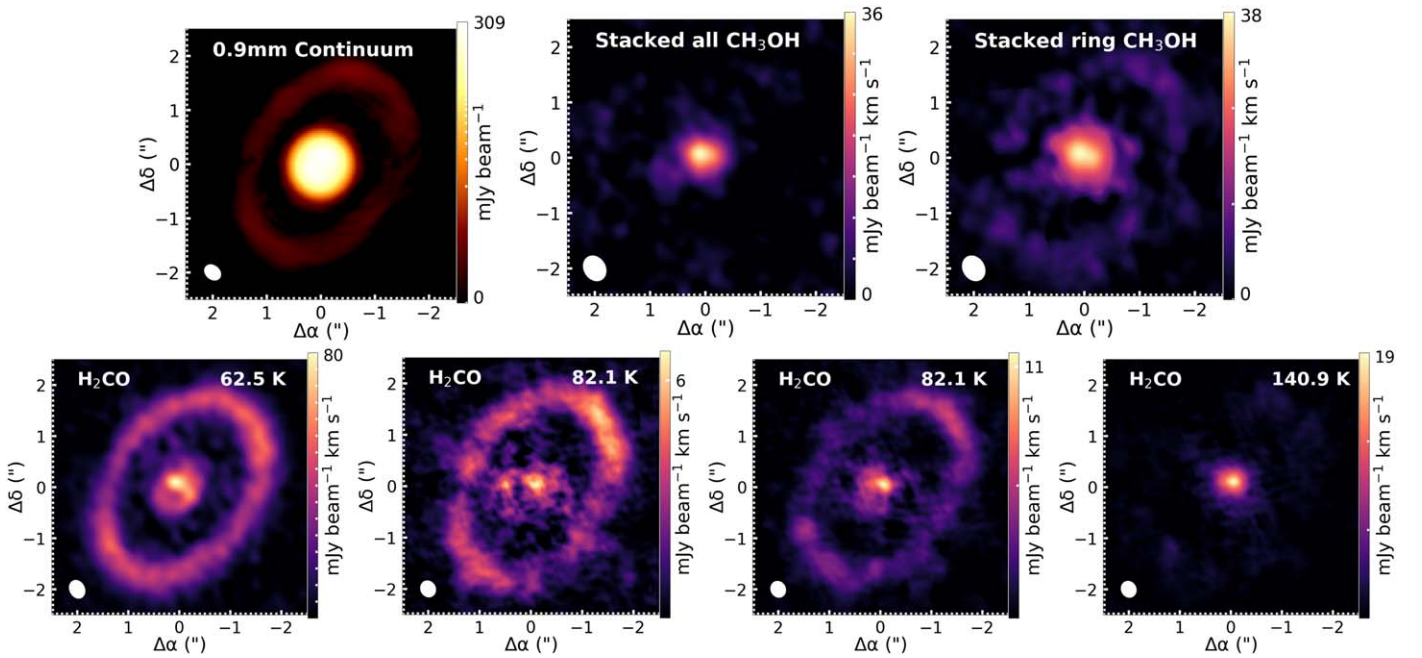


**Figure 1.** Top-left panel: dust continuum at 0.9 mm from the HD 100546 protoplanetary disk first published in A. S. Booth et al. (2024a) and plotted on a log scale to highlight the outer ring of continuum emission. Top-middle panel: stacked integrated intensity map generated using all 10 detected  $\text{CH}_3\text{OH}$  lines. Top-right panel: stacked integrated intensity map combining only the four  $\text{CH}_3\text{OH}$  lines that are detected in the outer ring. These data are presented with a stretched color scale to improve the visibility of the outer ring of emission. Bottom row: integrated intensity maps of the four detected  $\text{H}_2\text{CO}$  lines for the coolest transition (left) to the hottest transition (right). Note that there are two  $\text{H}_2\text{CO}$  transitions at 82.1 K ( $4_{2,3}-3_{2,2}$  and  $4_{2,2}-3_{2,1}$ ) and both are presented here. The synthesized beam is represented by the white ellipse in the bottom-left corner of each panel.

Five  $\text{H}_2\text{CO}$  lines were detected in the Cycle 7 data set at an S/N of at least 3; the parameters for these are also listed in Table 1. Note that two of the  $\text{H}_2\text{CO}$  lines detected in the Cycle 7 observations at approximately 291.38 GHz are blended with each other. We chose to keep these lines in our analysis to include a higher energy line ( $E_u = 141$  K) in the generated rotational diagram, which puts tighter constraints on our derived values for rotational temperature and column density.

### 3. Emission Morphology

In Figure 1 we present a selection of integrated intensity or moment 0 maps (generated using the aforementioned Keplerian mask and the `immoments` task in CASA with no noise clip) to show the emission morphology of the  $\text{CH}_3\text{OH}$  (top row) and  $\text{H}_2\text{CO}$  (bottom row) lines detected toward the HD 100546 disk in comparison with the dust continuum at 0.9 mm (top-left panel). There are two components of molecular emission that follow the ringed dust substructures: one component that is compact and lying within the inner  $\sim 100$  au, the other coincident with the previously observed outer dust ring centered at  $\sim 220$  au. Emission from the highest-energy  $\text{H}_2\text{CO}$  line ( $E_u = 140.9$  K; bottom-right panel) is bright only in the central compact component, whereas emission from the lowest-energy  $\text{H}_2\text{CO}$  line ( $E_u = 62.5$  K; bottom-left panel) also reveals emission from the outer ringed component. The line emission morphologies demonstrate the expected decreasing temperature gradient from the inner to the outer disk.

In Figure 1 we also show two stacked  $\text{CH}_3\text{OH}$  maps, generated using the `immath` task in CASA, to boost the S/N in the images of the weaker  $\text{CH}_3\text{OH}$  lines. The first stacked image (top-middle panel) was created using all 10 detected lines (listed in Table 1) and better highlights the inner compact

component. However, the outer component is faint in this image, as not all transitions are excited in the outer ring. We checked for extended emission using the spectral stacking technique implemented by the `gofish` package (R. Teague 2019). This method of azimuthally averaging the data increases the effective S/N. From this analysis, we find that four lines have significant emission peaking in a ring at  $\sim 220$  au (see Figure 2). These four lines also have the lowest upper-energy values ( $< 80$  K) of the 10 detected lines. To show the morphology of this ringed emission more clearly, we stack these four images only in the second stacked image (top-right panel). This map reveals that the gas-phase methanol also traces both the compact inner emission component as well as the one coinciding with the outer millimeter dust ring. Separate moment 0 maps for all 10  $\text{CH}_3\text{OH}$  transitions can be found in Appendix A (Figure 7).

The top panels of Figure 3 show the azimuthally averaged radial profiles, generated by radially binning the emission (with bin size approximately equal to half of the beam size) and then averaging (see A. S. Booth et al. 2024a), for the four  $\text{CH}_3\text{OH}$  lines with detections of both emission components. These transitions are those that have been stacked in the top-right panel in Figure 1. The bottom panels of Figure 3 show azimuthally averaged radial profiles for all detected  $\text{H}_2\text{CO}$  lines. The radial profiles for both molecules show the presence of two components of emission: a compact emission component that drops to a small or negligible value beyond approximately 110 au, as well as a ring peaking at around 200 au, which is within the range of radii at which the emission peaks depending on semimajor axis projections (see D. Fedele et al. 2021). Appendix B (Figure 8) shows the azimuthally averaged radial profiles for all  $\text{CH}_3\text{OH}$  lines in our sample.

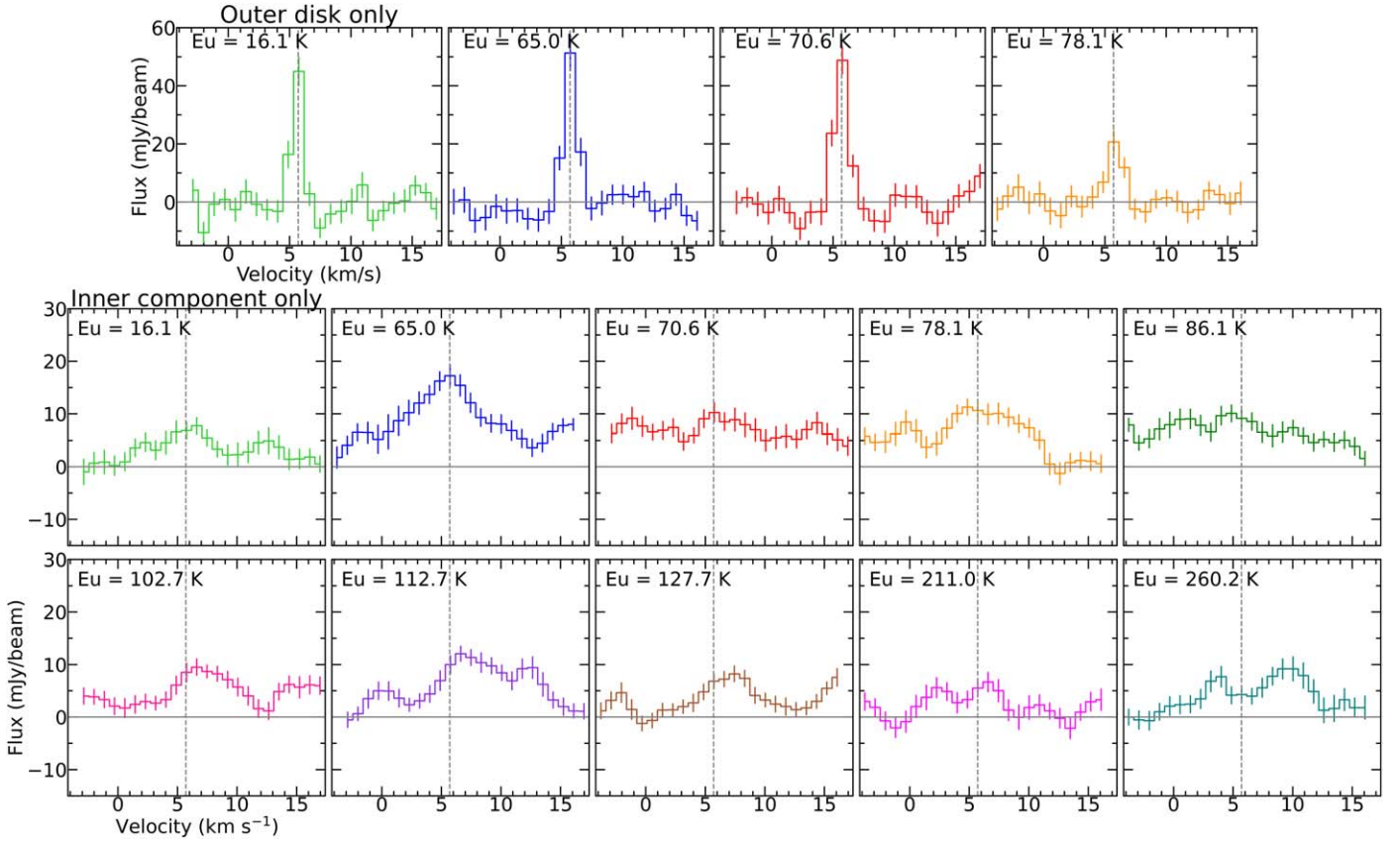


**Figure 2.** Top row: spectral line profiles for the four CH<sub>3</sub>OH lines that show emission from the outer ringed component according to the radial profiles in Figure 3. These spectral lines have been generated by integrating the emission between 180 and 260 au. Bottom two rows: spectral lines extracted for all 10 detected CH<sub>3</sub>OH lines generated from integrating the emission within 110 au. The dashed line represents the  $v_{\text{LSR}}$  of this source (5.7 km s<sup>-1</sup>).

**Table 1**  
H<sub>2</sub>CO and CH<sub>3</sub>OH Lines Used in the Rotational Diagram Analysis

Molecule	Transition	Frequency (GHz)	$E_u$ (K)	$g_u$	$A_{ul}$ (s <sup>-1</sup> )	Beam	Robust	Peak S/N <sup>a</sup>
2019.1.00193.S								
p-H <sub>2</sub> CO	4 <sub>2,3</sub> -3 <sub>2,2</sub>	291.238	82.1	9	$5.21 \times 10^{-4}$	0''33 × 0''29 (28°)	2.0	18
p-H <sub>2</sub> CO	4 <sub>2,2</sub> -3 <sub>2,1</sub>	291.948	82.1	9	$5.25 \times 10^{-4}$	0''33 × 0''29 (28°)	2.0	9
o-H <sub>2</sub> CO <sup>b</sup>	4 <sub>3,2</sub> -3 <sub>3,1</sub>	291.380	140.9	27	$3.04 \times 10^{-4}$	0''33 × 0''29 (28°)	2.0	4
o-H <sub>2</sub> CO <sup>b</sup>	4 <sub>3,1</sub> -3 <sub>3,0</sub>	291.384	140.9	27	$3.04 \times 10^{-4}$	0''33 × 0''29 (27°)	2.0	8
2021.1.00738.S								
o-H <sub>2</sub> CO	5 <sub>1,5</sub> -4 <sub>1,4</sub>	351.768	62.5	33	$1.20 \times 10^{-3}$	0''37 × 0''30 (27°)	0.5	57
CH <sub>3</sub> OH-A	1 <sub>1,1</sub> -0 <sub>0,0</sub>	350.905	16.1	12	$3.32 \times 10^{-4}$	0''47 × 0''37 (31°)	2.0	7
	7 <sub>0,7</sub> -6 <sub>0,6</sub>	338.408	65.0	60	$1.70 \times 10^{-4}$	0''48 × 0''39 (32°)	2.0	10
	7 <sub>2,5</sub> -6 <sub>2,4</sub>	338.640	102.7	60	$1.58 \times 10^{-4}$	0''48 × 0''39 (32°)	2.0	8
	13 <sub>0,13</sub> -12 <sub>1,12</sub>	355.603	211.0	108	$1.27 \times 10^{-4}$	0''45 × 0''32 (58°)	2.0	5
	14 <sub>1,13</sub> -14 <sub>0,14</sub>	349.107	260.2	116	$2.20 \times 10^{-4}$	0''47 × 0''37 (31°)	2.0	11
CH <sub>3</sub> OH-E	7 <sub>1,7</sub> -6 <sub>1,6</sub>	338.345	70.6	60	$1.67 \times 10^{-4}$	0''48 × 0''39 (32°)	2.0	8
	7 <sub>0,7</sub> -6 <sub>0,6</sub>	338.124	78.1	60	$1.70 \times 10^{-4}$	0''48 × 0''39 (32°)	2.0	9
	7 <sub>1,6</sub> -6 <sub>1,5</sub>	338.614	86.1	60	$1.71 \times 10^{-4}$	0''48 × 0''39 (32°)	2.0	9
	7 <sub>3,5</sub> -6 <sub>3,4</sub>	338.583	112.7	60	$2.69 \times 10^{-4}$	0''48 × 0''39 (32°)	2.0	8
	7 <sub>3,4</sub> -6 <sub>3,3</sub>	338.560	127.7	60	$1.40 \times 10^{-4}$	0''48 × 0''39 (32°)	2.0	6

**Notes.**

<sup>a</sup> As estimated from the channel maps.

<sup>b</sup> Sufficiently close to one another to be blended in the inner disk.

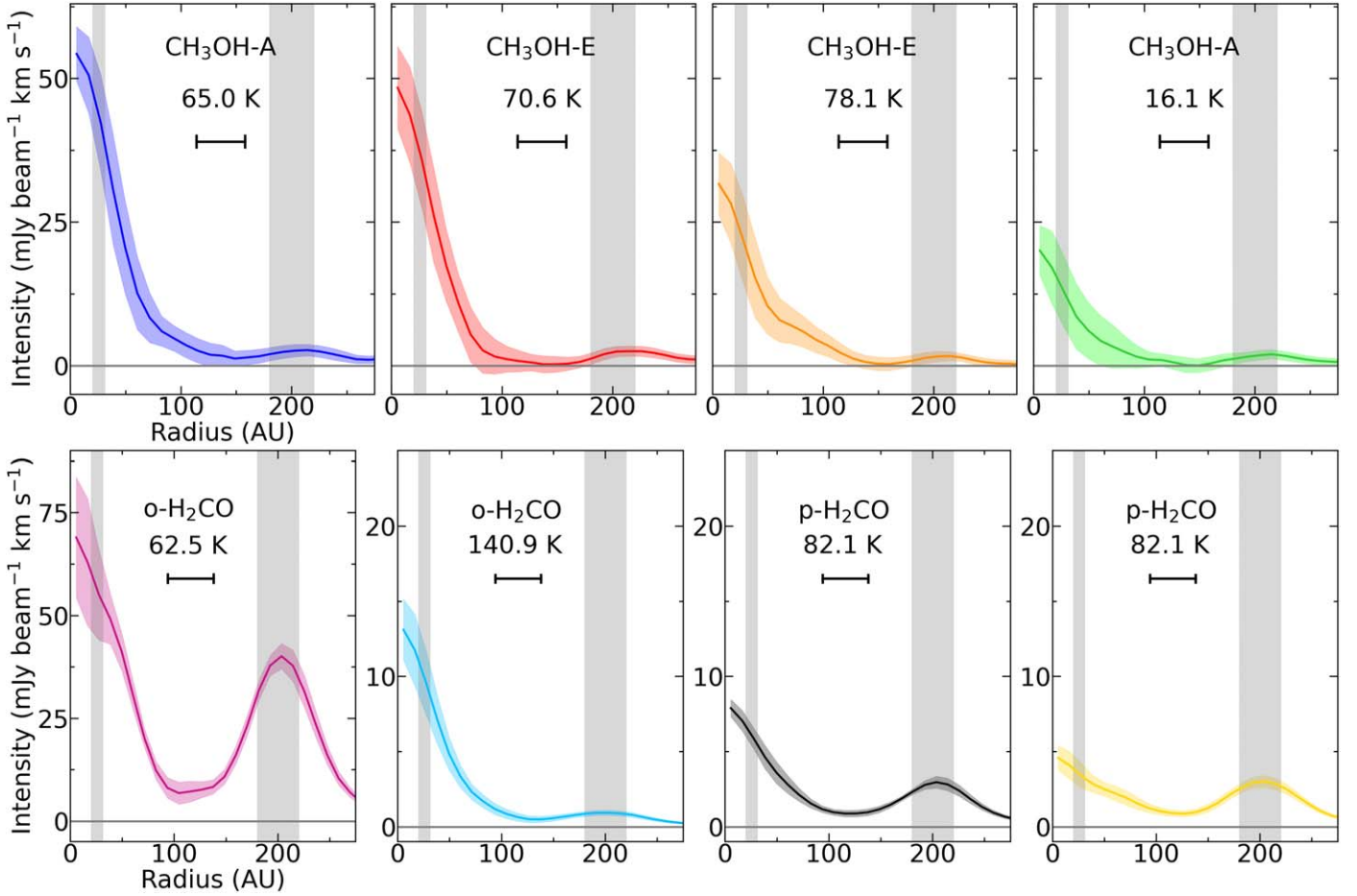


**Figure 3.** Azimuthally averaged radial profiles for four unblended  $\text{CH}_3\text{OH}$  lines (top row) and all  $\text{H}_2\text{CO}$  lines (bottom row) in order of decreasing peak intensity. These four  $\text{CH}_3\text{OH}$  lines are those that show both an inner compact and outer ringed component of emission. The latter coincides with the position of the dust ring, which peaks between approximately 180 and 220 au; the radial ranges of the peaks of the two dust rings seen in the 0.9 mm continuum emission between  $\sim 20$ –31 au and  $\sim 180$ –220 au are denoted by the gray shaded regions. Note that the  $\text{o-H}_2\text{CO}$  profile at 231.38 GHz contains contributions from two lines with equal transition properties: one at 291.380 GHz and one at 291.384 GHz. The horizontal bar shows the FWHM of the synthesized beam.

## 4. Methodology

### 4.1. Flux Extraction and Error Estimation

To investigate the two emission components seen in the integrated intensity maps shown in Section 3, we perform the described rotational diagram analysis for two radial ranges. For the inner compact emission component, we adopt  $r$  over the range 0–110 au, while for the outer ringed emission component, we adopt  $r$  over the range 180–260 au; according to Figure 3, in between these radial ranges, the flux from both  $\text{H}_2\text{CO}$  and  $\text{CH}_3\text{OH}$  drops to negligible values. We calculate values of  $7 \times 10^{-11}$  sr and  $2 \times 10^{-10}$  sr, for the solid angles of the inner and outer components, respectively, accounting for the fact that the outer component is an annulus.

Several of the spws of our Cycle 8 data have evidence of line emission from other species (with Keplerian motion evident in the channel maps), or possible multiple velocity components of  $\text{CH}_3\text{OH}$  due to, e.g., a disk wind or outflow. However, the weak S/N of these lines prevents us from readily distinguishing between these hypotheses, therefore we leave this to future work. To ensure flux extraction only from the line of interest centered on the source velocity, we applied a velocity clip when extracting the line fluxes:  $-0.6 \text{ km s}^{-1}$ – $12.0 \text{ km s}^{-1}$  for the inner region and  $4.5$ – $6.9 \text{ km s}^{-1}$  for the outer region. For reference, the  $v_{\text{LSR}}$  of this source is  $5.7 \text{ km s}^{-1}$  (C. Walsh et al.

2017). We adopt the same velocity ranges for the  $\text{H}_2\text{CO}$  lines; however, recall that there are two  $\text{o-H}_2\text{CO}$  lines at approximately 291.38 GHz that are separated only by approximately  $5 \text{ km s}^{-1}$ . This separation is sufficient for the lines to be blended in the spectrum extracted from the inner region (see Figure 9 in Appendix C), while being well separated in the spectrum extracted from the outer region (see Figure 10 in Appendix C). These two  $\text{o-H}_2\text{CO}$  transitions have identical  $A_{\text{ul}}$ ,  $g_{\text{u}}$  and  $E_{\text{u}}$  values (see Table 1), therefore we assume that they contribute equally to the total flux extracted from the inner component using the same velocity clip as for the  $\text{CH}_3\text{OH}$  emission extracted from the inner region. In the outer region, on the other hand, we adopt velocity clips from  $4.4$ – $6.7 \text{ km s}^{-1}$  and from  $8.3$ – $10.0 \text{ km s}^{-1}$ , to extract flux from the lines at 291.384 GHz and 291.380 GHz, respectively.

We use *gofish* to extract the line spectra for all  $\text{H}_2\text{CO}$  and  $\text{CH}_3\text{OH}$  lines for both the inner and outer components of emission from the disk. To calculate the total line flux, we then integrate over the line spectra extracted using *gofish* using numerical integration. Due to Keplerian line broadening and beam smearing in the inner disk, we cannot exploit the shift and stack method to extract the spectra here. To test the accuracy of *gofish* for spectral (and flux) extraction for the inner unresolved emission, we performed parallel spectral extraction using the *specflux* tool within CASA, adopting



**Table 2**Integrated Line Fluxes ( $S_\nu\Delta\nu$ ), Column Density in the Upper Energy Level ( $N_u$ ) and Line Opacity ( $\tau$ ) for the Inner (0–110 au) and Outer (180–260 au) Components of Emission

Molecule	Transition	Frequency (GHz)	$n_{\text{CR}}$ ( $\text{cm}^{-3}$ )	$S_\nu\Delta\nu$		$N_u$		$\tau$	
				(mJy km s $^{-1}$ )		(cm $^{-2}$ )			
				Inner	Outer	Inner	Outer	Inner	Outer
p-H <sub>2</sub> CO <sup>a</sup>	4 <sub>2,3</sub> -3 <sub>2,2</sub>	291.238	$6.2 \times 10^6$	$59 \pm 6$	$94 \pm 9$	$(9.8 \pm 1.0) \times 10^{10}$	$(5.3 \pm 0.5) \times 10^{10}$	0.008	0.03
	4 <sub>2,2</sub> -3 <sub>2,1</sub>	291.948	$6.3 \times 10^6$	$46 \pm 5$	$121 \pm 12$	$(7.7 \pm 0.8) \times 10^{10}$	$(6.9 \pm 0.7) \times 10^{10}$	0.008	0.03
o-H <sub>2</sub> CO <sup>a</sup>	4 <sub>3,2</sub> -3 <sub>3,0</sub>	291.380	$7.4 \times 10^6$	$38 \pm 4^b$	$26 \pm 3^c$	$(1.1 \pm 0.1) \times 10^{11}$	$(2.5 \pm 0.3) \times 10^{10}$	0.006	0.007
	4 <sub>3,1</sub> -3 <sub>3,0</sub>	291.384	$7.4 \times 10^6$	$38 \pm 4^b$	$31 \pm 3$	$(1.1 \pm 0.1) \times 10^{11}$	$(3.0 \pm 0.3) \times 10^{10}$	0.006	0.007
	5 <sub>1,5</sub> -4 <sub>1,4</sub>	351.768	$2.4 \times 10^6$	$498 \pm 50$	$1991 \pm 199$	$(3.6 \pm 0.4) \times 10^{11}$	$(4.9 \pm 0.5) \times 10^{11}$	0.06	0.3
CH <sub>3</sub> OH-A	1 <sub>1,1</sub> -0 <sub>0,0</sub>	350.905	...	$45 \pm 19$	$73 \pm 8$	$(1.2 \pm 0.5) \times 10^{11}$	$(6.5 \pm 0.7) \times 10^{10}$	0.003	0.007
	7 <sub>0,7</sub> -6 <sub>0,6</sub>	338.408	$4.0 \times 10^6$	$137 \pm 19$	$67 \pm 8$	$(6.9 \pm 1.0) \times 10^{11}$	$(1.2 \pm 0.1) \times 10^{11}$	0.006	0.008
	7 <sub>2,5</sub> -6 <sub>2,4</sub>	338.640	$3.6 \times 10^6$	$69 \pm 19$	...	$(3.8 \pm 1.1) \times 10^{11}$	...	0.004	...
	13 <sub>0,13</sub> -12 <sub>1,12</sub>	355.603	$3.2 \times 10^7$	$51 \pm 19$	...	$(3.5 \pm 1.3) \times 10^{11}$	...	0.003	...
	14 <sub>1,13</sub> -14 <sub>0,14</sub>	349.107	...	$75 \pm 19$	...	$(2.9 \pm 0.8) \times 10^{11}$	...	0.004	...
CH <sub>3</sub> OH-E	7 <sub>1,7</sub> -6 <sub>1,6</sub>	338.345	$1.3 \times 10^8$	$96 \pm 19$	$84 \pm 8$	$(4.9 \pm 1.0) \times 10^{11}$	$(1.5 \pm 0.1) \times 10^{11}$	0.006	0.007
	7 <sub>0,7</sub> -6 <sub>0,6</sub>	338.124	$1.3 \times 10^8$	$105 \pm 19$	$38 \pm 8$	$(5.3 \pm 1.0) \times 10^{11}$	$(6.8 \pm 1.4) \times 10^{10}$	0.006	0.006
	7 <sub>1,6</sub> -6 <sub>1,5</sub>	338.614	$1.3 \times 10^8$	$110 \pm 19$	...	$(5.5 \pm 1.0) \times 10^{11}$	...	0.005	...
	7 <sub>3,5</sub> -6 <sub>3,4</sub>	338.583	$1.1 \times 10^8$	$103 \pm 19$	...	$(3.3 \pm 0.6) \times 10^{11}$	...	0.007	...
	7 <sub>3,4</sub> -6 <sub>3,3</sub>	338.560	$1.1 \times 10^8$	$51 \pm 19$	...	$(3.1 \pm 1.2) \times 10^{11}$	...	0.003	...

**Notes.**<sup>a</sup> The uncertainty values for the H<sub>2</sub>CO lines have been calculated assuming an uncertainty of 10%.<sup>b</sup> These two Cycle 7 o-H<sub>2</sub>CO lines are blended in the inner region but not the outer region; hence, the inner region fluxes for these two lines were assumed to have equal contributions to the total measured flux.<sup>c</sup> The blended o-H<sub>2</sub>CO lines are well separated in the outer region but appear in the same spw; therefore, a separate velocity clip between 8.3 and 10.0 km s $^{-1}$  is used to measure the flux of this second line.

an aperture of 1'' in radius to cover the radial extent (110 au) of the inner component of emission. Both methods return consistent results (within the uncertainties); thus, we proceeded with *gofish* for all lines in order to use a consistent method. The bottom panels of Figure 2 show the extracted spectra using *gofish* for all CH<sub>3</sub>OH transitions observed in the inner disk.

We opt to use conservative estimates for the uncertainties in the line fluxes ( $S_\nu\Delta\nu$ ) because the statistical uncertainties provided by *gofish* (around 2–3 mJy km s $^{-1}$ ) are likely to be underestimated. To do this we extract the rms noise,  $\sigma$ , from a line-free channel of a noncontaminated spw (centered at 342.730 GHz) using *specflux* with an elliptical aperture of 4'' (covering the full disk) and calculate the uncertainty as  $\sigma\sqrt{n_{\text{chan}}}\Delta\nu$  where  $n_{\text{chan}}$  is the number of channels integrated over for each spectral line, while  $\Delta\nu$  is the velocity resolution (0.9 km s $^{-1}$ ). Our H<sub>2</sub>CO lines come from two different ALMA data sets, therefore we also include a flux uncertainty of 10% to account for any differences in the flux calibration between ALMA data sets.

The fluxes integrated over each emitting area ( $S_\nu\Delta\nu$ ) and their estimated uncertainties, along with the column densities in the upper energy level ( $N_u$ ) as calculated using Equation (4), are listed in Table 2 for all lines.

#### 4.2. Rotational Diagram Analysis

As discussed in the previous Section, we have detected 10 unblended transitions of CH<sub>3</sub>OH spanning  $E_u$  values from 16–260 K and four transitions of H<sub>2</sub>CO with  $E_u$  values ranging between 63 and 141 K. Hence, we can construct a rotational diagram and estimate the rotational temperature and column density for the two components of emission (inner and outer) for both species under the assumption of local thermal

equilibrium (LTE) and optically thin emission (P. F. Goldsmith & W. D. Langer 1999). Following the approach of R. A. Loomis et al. (2018) and J. D. Ilee et al. (2021), we use Equation (4) to calculate the column density in the upper energy level,  $N_u^{\text{thin}}$  (cm $^{-2}$ ),

$$N_u^{\text{thin}} = \frac{4\pi S_\nu \Delta\nu}{A_{ul} \Omega h c}. \quad (4)$$

In Equation (4),  $A_{ul}$  is the Einstein A coefficient for spontaneous emission (s $^{-1}$ ), while  $h$  and  $c$  represent Planck's constant and the speed of light, respectively, both in cgs units.  $S_\nu\Delta\nu$  represents the integrated flux density (measured in Jy km s $^{-1}$  and converted to cgs units), while  $\Omega$  is the solid angle (steradians) subtended by the emission, where the surface brightness  $I_\nu = S_\nu/\Omega$ . The solid angle is calculated using  $\Omega = (\pi r^2)/d^2$ , where  $r$  is the radial extent of the emission, while  $d$  is the distance to the source, taken as 110 pc (C. Wic-hittanakom et al. 2020), both converted into centimeters. The column density in the upper energy level,  $N_u^{\text{thin}}$ , can then be related to the total column density,  $N_T$ , assuming a Boltzmann distribution,

$$\frac{N_u^{\text{thin}}}{g_u} = \frac{N_T}{Q(T_{\text{rot}})} e^{-\frac{E_u}{k_B T_{\text{rot}}}}, \quad (5)$$

where  $Q(T_{\text{rot}})$  is the partition function at the rotational temperature, while  $k_B$  is Boltzmann's constant. We use precomputed partition functions as a function of temperature interpolated from CDMS (H. S. P. Müller et al. 2001; H. S. Müller et al. 2005; C. P. Endres et al. 2016) for both species. Note that this database assumes an ortho-to-para ratio

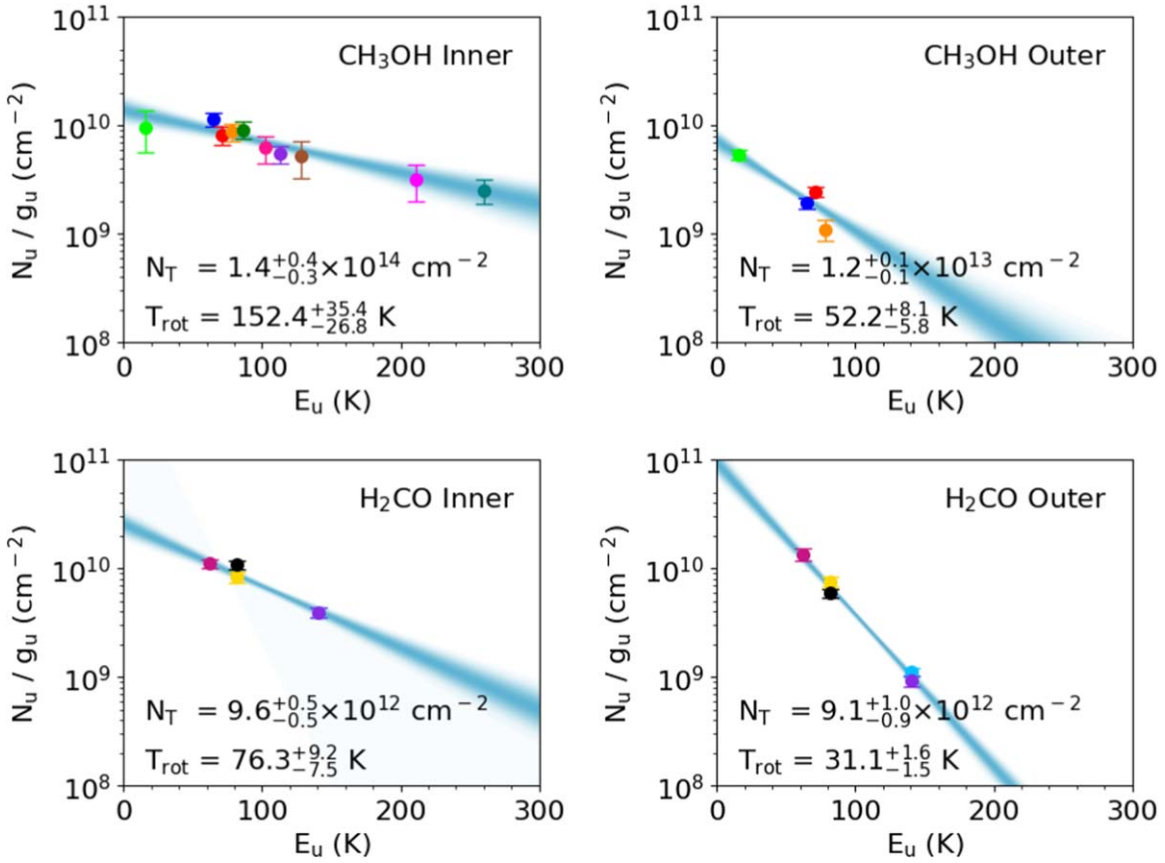


**Figure 4.** Best-fit rotational diagrams for CH<sub>3</sub>OH (top row) and H<sub>2</sub>CO (bottom row) for the inner (left panels) and outer (right panels) components of emission in the disk around HD 100546. The color of each point corresponds to the color of each transition as denoted in Figures 2 and 3. The two H<sub>2</sub>CO transitions at 291.38 GHz are well separated in the outer region, as shown in Appendix C (Figure 10) and are thus denoted separately by blue and purple points in the bottom-right panel; however, they are blended in the inner region and are thus represented by a single blue point in the bottom-left panel.

of 3 for H<sub>2</sub>CO. Taking the logarithm of Equation (5) converts this expression into a linear form,

$$\ln \frac{N_u^{\text{thin}}}{g_u} = \ln N_T - \ln Q(T_{\text{rot}}) - \frac{E_u}{k_B T_{\text{rot}}} \quad (6)$$

allowing extraction of the rotational temperature ( $T_{\text{rot}}$ ) and the total column density ( $N_T$ ). To do this, we use a Markov Chain Monte Carlo (MCMC) fitting procedure using the `emcee` Python module (D. Foreman-Mackey et al. 2013) with our measured  $S_\nu \Delta \nu$  values as input values. We also test our assumption of optically thin emission by applying an optical depth correction factor,

$$C_\tau = \frac{\tau}{1 - e^{-\tau}}, \quad (7)$$

where  $\tau$  is the line optical depth such that the true column density in the upper energy level is  $N_u = N_u^{\text{thin}} C_\tau$ . This modifies the left-hand side of Equation (6) to  $\ln N_u/g_u + \ln C_\tau$ , which is also fit in the MCMC routine. For this routine, our  $N_T$  priors are set to values between  $10^6 \text{ cm}^{-2}$  and  $10^{14} \text{ cm}^{-2}$  for H<sub>2</sub>CO in the outer region, between  $10^6 \text{ cm}^{-2}$  and  $10^{15} \text{ cm}^{-2}$  for H<sub>2</sub>CO in the inner region and between  $10^6 \text{ cm}^{-2}$  and  $10^{18} \text{ cm}^{-2}$  for both components of CH<sub>3</sub>OH. For the inner region, the  $T_{\text{rot}}$  priors are set to values between 15 and 300 K for both molecules, while for the outer region, they are set to values between 5 and 100 K. We run the MCMC for

1500 steps total, with 1000 removed as burn-in. We run this with 300 walkers in all cases, with the likelihood function built using Equation (6), which generates posterior probability distributions; the best-fit value is chosen as the median of this distribution, while the 16th–84th percentile forms the uncertainty range.

## 5. Results

We use the MCMC code and methodology described in Section 4 for both species, for both the inner and outer components of emission, which results in four best-fit rotational diagrams constraining the total column density ( $N_T$ ), rotational temperature ( $T_{\text{rot}}$ ) and line opacity for each case. We find that all of our detected lines are optically thin (see Table 2). The rotational diagrams and fitted parameters are shown in Figure 4, while the corner plots generated from the MCMC fitting are shown in Appendix D (Figure 11). Note that the fluxes for the o-H<sub>2</sub>CO lines at approximately 291.38 GHz are both included in the rotational diagrams, although they appear as a single point due to their identical  $E_u$  value (141 K). The MCMC results reveal a strong gradient in the temperature from the inner to the outer disk and show that the CH<sub>3</sub>OH emission is hotter than the relative H<sub>2</sub>CO emission in both components. In addition, we note the lack of scatter in both CH<sub>3</sub>OH rotational diagrams, suggesting that this emission is in LTE up to the highest critical density transitions; from this, it would be possible to directly estimate a lower limit for the gas density.



**Table 3**

$T_{\text{rot}}$  Values as Obtained Using the Rotational Diagram Analysis Compared to Gas Temperatures Measured in the Disk Midplane and Atmosphere by M. Kama et al. (2016)

Species	Inner $T_{\text{rot}}$ (K)	Outer $T_{\text{rot}}$ (K)
CH <sub>3</sub> OH	$152^{+35}_{-27}$	$52^{+8}_{-6}$
H <sub>2</sub> CO	$76^{+9}_{-8}$	$31^{+2}_{-2}$
Region	Inner $T_{\text{rot}}$ (K)	Outer $T_{\text{rot}}$ (K)
Midplane <sup>a</sup>	50–600	20–30
Atmosphere <sup>a</sup>	100–600	~100

**Note.**

<sup>a</sup> M. Kama et al. (2016).

We use Equation (8), with Einstein coefficients ( $A_{ul}$ ) from the LAMDA molecular database (F. L. Schöier et al. 2005) and collisional coefficients ( $C_{ui}$ ) from D. Rabli & D. R. Flower (2010) for H<sub>2</sub>CO and L. Wiesenfeld & A. Faure (2013) for CH<sub>3</sub>OH, to calculate the critical density ( $n_{\text{CR}}$ ) for each transition; we list these values in Table 2.

$$n_{\text{CR}} = \frac{A_{ul}}{\sum_i C_{ui}} \quad (8)$$

Here,  $A_{ul}$  (s<sup>-1</sup>) specifically refers to the Einstein coefficient between upper (u) and lower (l) levels, while  $\sum_i C_{ui}$  (cm<sup>3</sup> s<sup>-1</sup>) refers to the sum of collisional coefficients from an upper level (u) to all other lower levels (i). From our calculations, we obtain a lower limit for the gas density in the midplane of HD 100546 of order 10<sup>6</sup> cm<sup>-3</sup>; this is compatible with the models presented in M. Kama et al. (2016) and M. Leemker et al. (2024), in which the midplane gas density varies between 10<sup>8</sup> and 10<sup>10</sup> cm<sup>-3</sup>.

As shown in Table 3,  $T_{\text{rot}}$  for CH<sub>3</sub>OH is  $152^{+35}_{-27}$  K in the inner region and decreases to  $52^{+8}_{-6}$  K in the outer region.  $T_{\text{rot}}$  for H<sub>2</sub>CO is  $76^{+9}_{-8}$  K in the inner region and falls to  $31^{+2}_{-2}$  K in the outer region. We also compare these values with gas temperatures in the midplane and atmosphere of the disk as obtained by M. Kama et al. (2016). CH<sub>3</sub>OH has stronger binding to a multilayer surface than H<sub>2</sub>CO with measured binding energies of 3820 K and 3260 K (E. M. Penteadó et al. 2017), respectively. Hence, we expect that CH<sub>3</sub>OH will desorb at a higher temperature than H<sub>2</sub>CO and that it should have a higher rotational temperature if the bulk of the emission is arising from near the snowlines (or snow surfaces) for both species. In Appendix E (Figure 12), we calculate the expected desorption temperatures for CH<sub>3</sub>OH and H<sub>2</sub>CO, assuming a range of values for the gas density at the midplane of HD 100546 as modeled by M. Kama et al. (2016). We find that CH<sub>3</sub>OH will desorb above a temperature of 109 K for a gas density of 10<sup>12</sup> cm<sup>-3</sup> (M. Kama et al. 2016) and H<sub>2</sub>CO will desorb above a temperature of 93 K at the same density. Using a higher binding energy for CH<sub>3</sub>OH (e.g., 4931 K, as measured by W. A. Brown & A. S. Bolina 2007) leads to the desorption temperature of methanol changing to 140 K. We also find that, for the range of gas densities assumed, CH<sub>3</sub>OH will desorb at a higher temperature than H<sub>2</sub>CO by 14–16 K (M. P. Collings et al. 2004; J. A. Noble et al. 2012; E. M. Penteadó et al. 2017).

The fact that CH<sub>3</sub>OH has a higher  $T_{\text{rot}}$  overall than H<sub>2</sub>CO could be explained if CH<sub>3</sub>OH is surviving in the inner disk at higher temperatures than H<sub>2</sub>CO. Note that the computation of thermal desorption rates and desorption temperatures from binding energy values measured in the laboratory is more complex than is commonly assumed (M. Minissale et al. 2022; N. F. W. Ligterink & M. Minissale 2023).

The  $T_{\text{rot}}$  values in the inner component are explainable solely by thermal desorption, however, this is not the case for the lower  $T_{\text{rot}}$  values in the outer component. Here, the origin of the CH<sub>3</sub>OH emission is likely nonthermal desorption from the ice mantles on the dust grains, because gas-phase CH<sub>3</sub>OH does not have efficient gas-phase formation routes at low temperatures (R. Garrod et al. 2006; W. D. Geppert et al. 2006; C. Walsh et al. 2014). Sources of nonthermal desorption in the outer regions of protoplanetary disks are cosmic-rays, X-rays, UV photons (from the star and surrounding interstellar medium) and excess energy in grain-surface reactions (so-called reactive or chemical desorption; C. Walsh et al. 2014; H. M. Cuppen et al. 2017). It should be noted, however, that in the case of nonthermal desorption at low temperatures, it has been suggested by experimental studies that CH<sub>3</sub>OH does not desorb intact, which therefore inhibits the photodesorption yield of intact CH<sub>3</sub>OH under these conditions (M. Bertin et al. 2016; G. A. Cruz-Díaz et al. 2016; S. Notsu et al. 2021). We take this fragmentation of methanol ice upon photodesorption into account in our models (see M. Bertin et al. 2016). On the other hand, cold gas-phase H<sub>2</sub>CO has two potential origins: nonthermal desorption and gas-phase formation (R. A. Loomis et al. 2015; M. T. Carney et al. 2017; J. Terwisscha van Scheltinga et al. 2021).

The best-fit rotational diagrams show that the column density for CH<sub>3</sub>OH is higher than that for H<sub>2</sub>CO in the inner component. The CH<sub>3</sub>OH column density is also higher in the inner region than in the outer region ( $1.4^{+0.4}_{-0.3} \times 10^{14}$  cm<sup>-2</sup> versus  $1.2^{+0.1}_{-0.1} \times 10^{13}$  cm<sup>-2</sup>); however, the column density for H<sub>2</sub>CO is similar across the disk with values of  $9.6^{+0.5}_{-0.5} \times 10^{12}$  and  $9.1^{+1.0}_{-0.9} \times 10^{12}$  cm<sup>-2</sup> in the inner and outer components, respectively.

Using our fitted column densities, we can now constrain values for the CH<sub>3</sub>OH/H<sub>2</sub>CO ratio across the disk surrounding HD 100546. For the inner region, we obtain a value of  $14.6^{+5.2}_{-4.6}$ , while for the outer region we obtain a value of  $1.3^{+0.3}_{-0.2}$ . This order-of-magnitude difference in ratio supports the presence of two COM reservoirs in the disk surrounding HD 100546 with different chemical origins. Previously, A. S. Booth et al. (2024a) estimated the column density ratio for CH<sub>3</sub>OH/H<sub>2</sub>CO to be  $18 \pm 4$  in the inner disk and  $1.1 \pm 0.6$  for the outer ringed component, which is in good agreement with the results of the more quantitative analysis presented here.

## 6. Discussion

### 6.1. Rotational Temperature of CH<sub>3</sub>OH

The analysis presented in Section 5 shows that  $T_{\text{rot}}$  for CH<sub>3</sub>OH ranges from  $152^{+35}_{-27}$  K in the inner disk to  $52^{+8}_{-6}$  K in the outer ring. The rotational temperatures measured for the inner component for both species are consistent with what would be expected if the origin of the emission here were due to the thermal desorption from the ice phase to the gas phase, while the lower temperatures in the outer component are likely indicative of nonthermal desorption. Recently, J. D. Ilee et al.

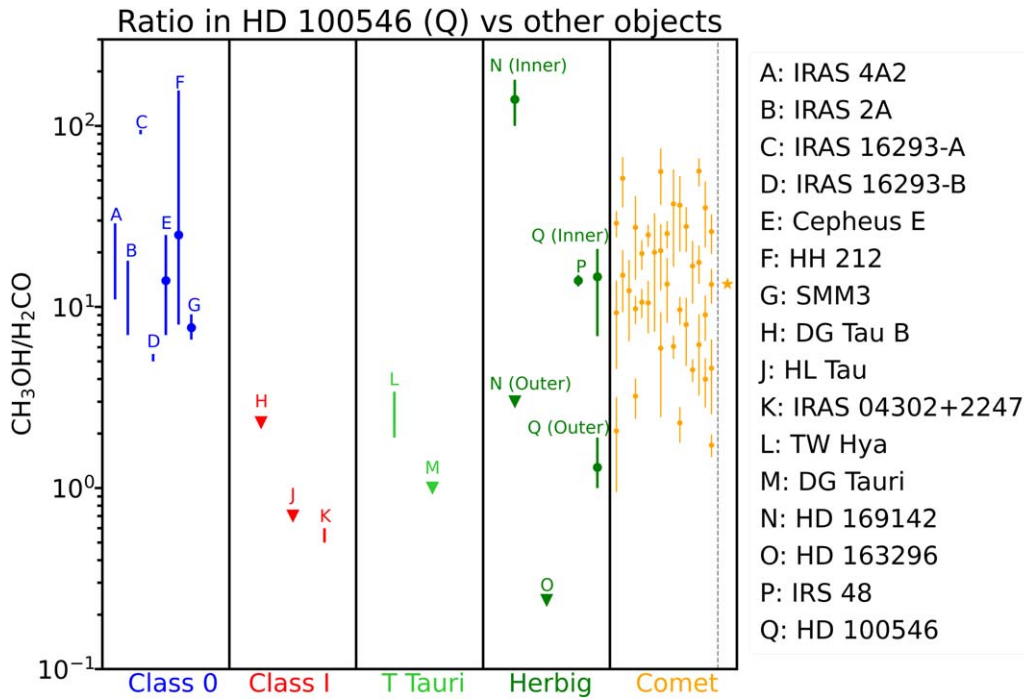


**Figure 5.**  $\text{CH}_3\text{OH}/\text{H}_2\text{CO}$  ratios measured toward the inner and outer regions of HD 100546 (Q) compared to values measured toward objects of varying evolutionary stages. Letters have been used to denote each object; refer to Appendix F (Table 4) for the reference(s) associated with each source. Note that circles represent values with error bars, bars represent a range, triangles represent upper-limit values for the  $\text{CH}_3\text{OH}/\text{H}_2\text{CO}$  ratios for DG Tau B (H), HL Tau (J), HD 163296 (O), as well as the outer region of HD 169142 (N), while the star represents the median value of measurements across a sample of 38 solar system comets (M. Lippi et al. 2024).

(2025, in preparation) conducted a multiline analysis in the disk around TW Hya and measured a  $T_{\text{rot}}$  for  $\text{CH}_3\text{OH}$  of  $36^{+25}_{-10}$  K. This is also in line with a source of  $\text{CH}_3\text{OH}$  gas arising from nonthermal desorption from icy dust grains, as suggested by astrochemical models. The lower rotational temperature for  $\text{CH}_3\text{OH}$  in TW Hya when compared to HD 100546 might reflect its generally cooler disk temperature (see, e.g., M. Kama et al. 2016). The only other disk in which  $T_{\text{rot}}$  has been empirically measured for  $\text{CH}_3\text{OH}$  is the disk around IRS 48. N. van der Marel et al. (2021) report a  $T_{\text{rot}}$  for  $\text{CH}_3\text{OH}$  of  $103^{+6}_{-5}$  K for IRS 48 compared with  $173^{+11}_{-9}$  K for  $\text{H}_2\text{CO}$ . This is the opposite trend to that seen in HD 100546 and is a trend that persists in a follow-up analysis published in M. Temmink et al. (2025), although it was noted in that work that there is large scatter in the  $T_{\text{rot}}$  for  $\text{CH}_3\text{OH}$ , which is likely due to subthermal excitation. In the IRS 48 disk, the  $\text{CH}_3\text{OH}$  and  $\text{H}_2\text{CO}$  emission are both strongly associated with a highly asymmetric dust trap thought to be caused by a vortex. The complex dynamics in this system may influence the thermal and chemical structure of the disk and give rise to the relative differences in  $T_{\text{rot}}$  for these two molecules when compared to HD 100546. Indeed, the  $T_{\text{rot}}$  value reported for  $\text{H}_2\text{CO}$  in IRS 48 is very high when compared to literature; our value of  $31^{+2}_{-2}$  K measured toward the outer region of HD 100546 is much more in line with values reported toward the outer regions of other disks. For example, C. Hernández-Vera et al. (2024a) measured a  $\text{H}_2\text{CO}$  rotational temperature of approximately 20 K for the disk around HD 163296, while the  $\text{H}_2\text{CO}$  disk survey by J. Pegues et al. (2020) found values between 10 and 40 K in four sources.

In Appendix F, we compare and discuss our results for  $T_{\text{rot}}$  with those reported in the literature for objects at different evolutionary stages of star and planet formation.

## 6.2. $\text{CH}_3\text{OH}/\text{H}_2\text{CO}$ Column Density Ratio

It is important to note that our observations are purely tracing the gas phase, so there is no guarantee that they are directly tracing the ice ratios. The inner region is thermally desorbed, therefore it is likely that the ice ratios are being traced here. However, in the outer region, we have nonthermal desorption in the form of photodesorption, for which the efficiencies are different for each species (M. Bertin et al. 2016; R. Martín-Doménech et al. 2016). Furthermore, we have the added complication of gas-phase  $\text{H}_2\text{CO}$  formation occurring in the outer region, which also reduces the likelihood that we can directly trace the ice ratios here. From our results, the column density for  $\text{CH}_3\text{OH}$  decreases by approximately 1 order of magnitude going from the inner to outer disk of HD 100546, while  $\text{H}_2\text{CO}$  has a similar column density in the two emission components. This is reflected in the  $\text{CH}_3\text{OH}/\text{H}_2\text{CO}$  column density ratio, which ranges from  $14.6^{+5.2}_{-4.6}$  in the inner disk to  $1.3^{+0.3}_{-0.2}$  in the outer disk. We compare our measured ratios for both components of emission in the disk around HD 100546 with representative values from younger objects, T Tauri and other Herbig objects, along with comets in Figure 5.

We reiterate that the successful detection of gas-phase  $\text{CH}_3\text{OH}$  in the HD 100546 disk was first reported in A. S. Booth et al. (2021). The values that we derive here are consistent with the radial column density ratio in that work, which were calculated assuming the same rotational temperature for both  $\text{H}_2\text{CO}$  and  $\text{CH}_3\text{OH}$  (which in turn was derived from a rotational diagram analysis for  $\text{H}_2\text{CO}$ ). Our results for the rotational temperature for  $\text{H}_2\text{CO}$  are also consistent with this previous work. The column densities and rotational temperatures derived in the present work have significantly smaller error bars due to the higher sensitivity and higher spatial resolution of these data, as well as the detection of

multiple lines of both species spanning a wider upper-energy-level range. Lower measured  $\text{CH}_3\text{OH}/\text{H}_2\text{CO}$  ratios have previously been attributed to more efficient gas-phase formation of  $\text{H}_2\text{CO}$ ; this has been observed for the T Tauri disk surrounding TW Hya (J. Terwisscha van Scheltinga et al. 2021) and a low upper limit to the ratio has been constrained for HD 163296 (M. T. Carney et al. 2019). Efficient gas-phase formation of  $\text{H}_2\text{CO}$  in the outer region of HD 100546 is a possible explanation for the constant column density observed across the disk, while the aforementioned low photodesorption rates of  $\text{CH}_3\text{OH}$  at low temperatures (M. Bertin et al. 2016; G. A. Cruz-Díaz et al. 2016; S. Notsu et al. 2021) may provide an explanation for the lower column density measured in the outer disk. Despite also being a Herbig Ae disk, HD 163296 is cold compared to HD 100546 and possesses a CO snowline at  $\sim 60$  au (C. Qi et al. 2011; K. Zhang et al. 2019, 2021). Modeling based on Herschel observations of the inner part of HD 163296 reveal high abundances of gas-phase  $\text{H}_2\text{O}$ , in contrast to HD 100546, where higher energy transitions of  $\text{H}_2\text{O}$  remain undetected (see L. M. Pirovano et al. 2022), which is proposed to be a consequence of differing chemical histories of the two disks, including pebble drift in HD 163296.

Comparing our column density ratios to those measured toward other Herbig disks, the ratio toward IRS 48 has been measured as  $14 \pm 1$ , which is close to the value measured toward the inner region of HD 100546. However, if the emission from  $\text{H}_2\text{CO}$  toward IRS 48 is optically thick, as is suggested by  $\text{H}_2^{13}\text{CO}$  observations (A. S. Booth et al. 2024b), as well as analysis of more recent  $\text{H}_2\text{CO}$  observations (M. Temmink et al. 2025), the ratio may be as low as 1, which is closer to our measured value for the outer region of HD 100546. Similar to HD 100546, the  $\text{CH}_3\text{OH}/\text{H}_2\text{CO}$  ratio also decreases from the inner to outer disk of HD 169142 (A. S. Booth et al. 2023b). The ratio measured toward the inner region of HD 169142 is an order of magnitude higher than that for HD 100546; however, the outer region upper limit (due to the nondetection of  $\text{CH}_3\text{OH}$ ) is consistent with our value for HD 100546. An upper-limit ratio of  $<0.24$  was measured toward the disk surrounding HD 163296 (M. T. Carney et al. 2019), which is lower than that seen toward the outer region of HD 100546 in the present work. Meanwhile, an outwardly decreasing trend is also seen in the Horsehead PDR, which has been shown to exhibit similar desorption behavior to protoplanetary disks, wherein the  $\text{CH}_3\text{OH}/\text{H}_2\text{CO}$  ratio decreases from  $\sim 1$  in the thermally desorbed core to  $\sim 0.5$  in the nonthermally desorbed PDR itself (V. V. Guzmán et al. 2013).

The differences in the ratios between different Herbig disks may be related to their structure as discussed above for HD 163296. IRS 48, HD 100546 and HD 169142 all possess significantly sized inner cavities that allow for direct exposure of the ice reservoir in the midplane to the stellar radiation driving thermal sublimation of the ices, thus revealing the presence of  $\text{CH}_3\text{OH}$ . However,  $\text{CH}_3\text{OH}$  was not detected in HD 142527, despite the presence of a cavity; this is likely due to the fact that, unlike other transition disks around Herbig stars, the dust trap (and the ice) is located much farther from the host star (peaking at  $\sim 175$  au) and so the conditions are too cold ( $\sim 40$  K) for thermal sublimation to take place (S. Casassus et al. 2013; M. Temmink et al. 2023). Whether or not an outer cooler component of  $\text{CH}_3\text{OH}$  emission is present will depend on the efficiency of nonthermal desorption in the outer regions of the disk.

Comparing the column density ratios for HD 100546 with values measured toward younger objects, as well as toward solar system comets (see Figure 5), the inner region of HD 100546 has a higher column density ratio than that found in the Class I objects IRAS 04302 (0.5–0.6; L. Podio et al. 2020), DG Tau B ( $<1.5$ –2.3; A. Garufi et al. 2020), as well as HL Tau ( $<0.7$ ; A. Garufi et al. 2022); these ratios are more similar to those measured toward the outer region of HD 100546, pointing to a similar chemical origin (nonthermal desorption and gas-phase formation of  $\text{H}_2\text{CO}$ ). On the other hand, abundance ratios measured in hot corinos surrounding Class 0 objects NGC 1333-IRAS 2A (V. Taquet et al. 2015), HH 212 (C.-F. Lee et al. 2022), Cep E-mm (J. Ospina-Zamudio et al. 2018), the protobinary IRAS 16293-2422 (M. V. Persson et al. 2018; S. Manigand et al. 2020), as well as the potential hot corino surrounding SMM3 (a protostellar core which is embedded in Orion B9; O. Miettinen 2016), range from 1–2 orders of magnitude higher than that measured toward HD 100546, while the shock-driven  $\text{CH}_3\text{OH}$  enhancement in the Class 0/I object BHB 07-11, which does not host a hot corino, leads to a ratio that is 3–4 orders of magnitude higher than HD 100546 (C. Vastel et al. 2022; L. Evans et al. 2023). These differences could indicate substantial chemical modification for both  $\text{CH}_3\text{OH}$  and  $\text{H}_2\text{CO}$  and/or diversity in chemical conditions in hot corinos and shocked regions compared with the inner regions of HD 100546. The inner region of HD 100546 has a more similar ratio to the median value measured across a sample of 38 solar system comets compiled by M. Lippi et al. (2024). That the ratio in the recently sublimated ice in the inner regions of HD 100546 is similar to the one in cometary ices further supports the hypothesis that a significant fraction of interstellar ice has been inherited and has survived transport through the HD 100546 protoplanetary disk.

### 6.3. Chemical Modeling

A. S. Booth et al. (2021) supplemented their observations with a chemical model of the disk to investigate the chemical origins of  $\text{CH}_3\text{OH}$ . They focused on whether it is possible that the observed  $\text{CH}_3\text{OH}$  formed in situ or was inherited from a previous evolutionary stage of the object. They assumed a 2D physical structure and number density of hydrogen nuclei ( $n_{\text{H}}$ ), gas and dust temperature, UV radiation field, as well as X-ray ionization rate as in M. Kama et al. (2016), with a cosmic-ray ionization rate of  $5 \times 10^{-17} \text{ s}^{-1}$ . They found that it was not possible to produce  $\text{CH}_3\text{OH}$  in situ in this disk under their assumption of atomic initial conditions. Moreover, the abundance of  $\text{CH}_3\text{OH}$  was found to decay in the disk over time because it cannot reform due to the warm temperature of the dust throughout the disk ( $\gtrsim 20$  K) that inhibits freeze-out of CO (M. Kama et al. 2016). Based on these results, they concluded that the  $\text{CH}_3\text{OH}$  observed toward HD 100546 was inherited from an earlier evolutionary phase. In addition, recent results from physicochemical modeling of the dust rings also agree that the disk surrounding HD 100546 is warm (M. Leemker et al. 2024); however, the CO map from the same paper suggests that freeze-out can occur in the outer regions of the disk, so there is the possibility for methanol reformation on the dust grains at the location of the outer dust ring, which should be tested in future gas-grain models.

Our constrained rotational temperatures for  $\text{CH}_3\text{OH}$  and  $\text{H}_2\text{CO}$  show two components of emission: one inner component driven by thermal desorption of ices and one outer



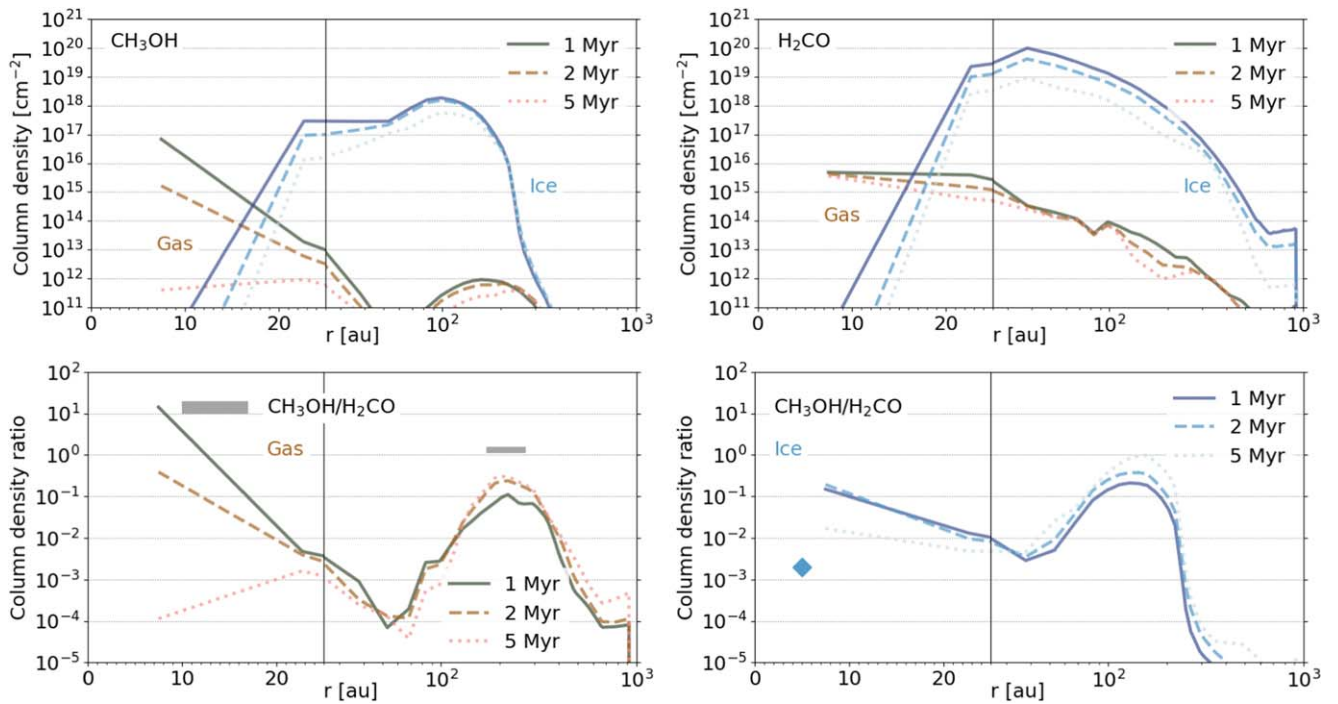


**Figure 6.** Top row: column density calculated as a function of radius averaged over 15 au wide radial bins for the disk around HD 100546 for  $\text{CH}_3\text{OH}$  (left panel) and  $\text{H}_2\text{CO}$  (right panel) at 1 (solid), 2 (dashed) and 5 (dotted) Myr. Bottom row:  $\text{CH}_3\text{OH}/\text{H}_2\text{CO}$  column density ratio calculated for the gas (left panel) and ice (right panel) phase, at 1 (solid), 2 (dashed) and 5 (dotted) Myr. The brown colors denote gas-phase molecules while the blue colors represent the ice phase. Note that the  $\text{CH}_3\text{OH}/\text{H}_2\text{CO}$  models plotted for the ice phase (bottom-right panel) are restricted to radii  $\geq 15$  au as the column density in the ice phase is negligible within this radius. The models within 25 au have been plotted on a linear scale to highlight the structure in the inner disk. The gray shaded regions on the bottom-left panel indicate the observed ratios derived in this work for the inner ( $15^{+3}_{-2}$ ) and outer ( $1.3^{+0.3}_{-0.2}$ ) components (note that the radial extent of the shaded regions is arbitrary and is set to guide the eye only). The diamond marker on the bottom-right panel indicates the initial abundance ratio for  $\text{CH}_3\text{OH}/\text{H}_2\text{CO}$  ice adopted in the chemical model ( $2 \times 10^{-3}$ ).

component driven by nonthermal desorption, as well as a gradient in the  $\text{CH}_3\text{OH}/\text{H}_2\text{CO}$  column density ratio across the disk. Here, we revisit the models presented in A. S. Booth et al. (2021) in light of the results reported here. Note that this physical model for HD 100546 comes from the thermochemical modeling results presented in M. Kama et al. (2016), which assumes a dust-to-gas mass ratio of 100 and uses the chemical network described in C. Walsh et al. (2015) and references therein. A more detailed description of the chemical model can also be found in Appendix G.

We show in Figure 6 the resultant predictions from our models for the radial column densities (top row) of both  $\text{CH}_3\text{OH}$  (left) and  $\text{H}_2\text{CO}$  (right) along with the resultant  $\text{CH}_3\text{OH}/\text{H}_2\text{CO}$  column density ratio (bottom row) for the gas (left) and ice (right) phases. To show a fair comparison to our observational results, the modeled column densities are first interpolated over a denser linear grid with 1 au resolution in radius, then averaged over 15 au radial bins. This is necessary because the original grid was constructed in log space with higher resolution in the inner regions versus the outer regions. The results from the model at its original grid resolution can be found in Appendix G (Figure 14).

The column densities in the top row of Figure 6 are extracted at a time of 1 (solid lines), 2 (dashed lines) and 5 (dotted lines) Myr for both the gas-phase (brown colors) and ice phase (blue colors). The model predicts an outwardly decreasing column density trend (although a slight increase is seen in the 5 Myr case within 25 au) toward a minimum ( $<10^{11} \text{ cm}^{-2}$ ) beyond 30–40 au, before rising again to reach a maximum ( $\sim 10^{12} \text{ cm}^{-2}$ ) in the outer disk colocated with the outer dust

ring. The  $\text{CH}_3\text{OH}$  ice retains a substantial column density of  $\sim 10^{16}–10^{18} \text{ cm}^{-2}$  between radii of  $\sim 20–220$  au; however, it does decrease with time. The primary source of gas-phase methanol in the inner disk is thermal desorption; the origin of the emission in the outer disk is photodesorption. This is supported by the distribution of the number density of gas-phase and ice-phase  $\text{CH}_3\text{OH}$  shown in Appendix G (Figure 15) as a function of radius,  $r$  and height divided by the radius,  $z/r$ . The gas-phase  $\text{CH}_3\text{OH}$  peaks in abundance just inside its snow surface at a temperature above 150 K, as shown in the top-right panel of Appendix G (Figure 15). This is in excellent agreement with the derived rotational temperature for  $\text{CH}_3\text{OH}$  in the inner disk. On the other hand, the spatial extent of ice-phase  $\text{CH}_3\text{OH}$  is set by the strength of the UV radiation field in the disk, with  $\text{CH}_3\text{OH}$  ice surviving only where the field strength is  $\lesssim 0.01$  times that of the interstellar radiation field. Gas-phase methanol reaches a reasonable abundance only at temperatures  $\lesssim 50$  K in the outer disk, also in excellent agreement with the rotational temperature derived from the observations.

The column density for  $\text{H}_2\text{CO}$  is predicted to have a much shallower radial abundance gradient, reflecting its efficient formation in both gas and ice. Similar to  $\text{CH}_3\text{OH}$ , its column density peaks just within the dust cavity reaching a maximum of  $\sim 10^{16} \text{ cm}^{-2}$ , declining steadily with radius before falling to low values ( $<10^{11} \text{ cm}^{-2}$ ) beyond  $\sim 500$  au. We can also see that what we can detect in the gas phase is only a small fraction of the total  $\text{H}_2\text{CO}$  in the disk, with the rest locked up in the form of ice in the outer disk. We also note that the physical disk model used here has not accounted for the gas and dust

substructure that we now know is present in the disk around HD 100546. Accounting for the presence of a gas cavity between 40 and 175 au, as was done in the recent models by M. Leemker et al. (2024) would likely shape the radial column density of  $\text{H}_2\text{CO}$  to produce a ring-like structure in the outer disk; we will test this in future models.

Appendix G (Figure 16) shows the abundance of gas-phase (left) and ice-phase (right)  $\text{H}_2\text{CO}$  at times of 1 (top), 2 (middle), and 5 (bottom) Myr, as a function of disk radius,  $r$ , as well as height divided by the radius,  $z/r$ . The distributions of gas-phase and ice-phase  $\text{H}_2\text{CO}$  are more extended than those for  $\text{CH}_3\text{OH}$ , supporting the notion that multiple chemical origins are contributing to their distribution. The abundance of gas-phase  $\text{H}_2\text{CO}$  peaks at temperatures  $\gtrsim 70$  K in the inner disk, in excellent agreement with the derived rotational temperature in this work. We also see good agreement between our results and the predicted snowline locations for both  $\text{CH}_3\text{OH}$  and  $\text{H}_2\text{CO}$  according to the model (150 and 70 K, respectively) in the inner component. However, while this prediction is also in good agreement for the outer component of  $\text{CH}_3\text{OH}$ , the obtained  $T_{\text{rot}}$  for the outer component of  $\text{H}_2\text{CO}$  suggests a deeper origin closer to the colder midplane, which is not in agreement with the modeling predictions presented in Appendix G (Figure 16). In addition to this, gas-phase  $\text{H}_2\text{CO}$  in the outer disk is distributed over a greater range of temperatures than that for  $\text{CH}_3\text{OH}$ , mainly at temperatures  $\gtrsim 40$  K, which is also somewhat in disagreement with the rotational temperature for  $\text{H}_2\text{CO}$  derived from the observations for the outer disk ( $31^{+2}_{-2}$  K). This could be as a result of the gas-phase formation of  $\text{H}_2\text{CO}$  being more efficient deeper in the disk than the nonthermal photodesorption of  $\text{H}_2\text{CO}$ , which has been formed via the grain surface, or the outer disk being cooler in the outer regions than suggested by the model from M. Kama et al. (2016). More tailored models are needed to investigate this further. In addition, the lowest  $E_u$   $\text{H}_2\text{CO}$  transition has an optical depth that is an order of magnitude higher than the other transitions in our sample (see Table 3), so this may result in a higher-than-expected value for  $T_{\text{rot}}$ . Indeed, more recent models of the HD 100546 disk by M. Leemker et al. (2024) suggest that the temperature in the disk midplane at the location of the outer dust ring reaches temperatures as low as 20 K, which is 10–15 K colder than the models used here. This is indicative of potential CO freeze-out in this region.

In the bottom row of Figure 6, we show the column density ratio ( $\text{CH}_3\text{OH}/\text{H}_2\text{CO}$ ) for the gas phase (left) and the ice phase (right) at time steps of 1, 2, and 5 Myr as predicted by the chemical model. The ratio for the gas in the inner disk within the cavity ranges from  $\sim 10^{-4}$  (5 Myr) to 10 (1 Myr) and that for the outer disk and colocated with the dust ring is  $\sim 0.1$ . The model therefore predicts a similar trend in  $\text{CH}_3\text{OH}/\text{H}_2\text{CO}$  with radius, albeit with a higher ratio in the inner disk and a lower ratio in the outer disk at 1 Myr. However, given that this model has not been tailored nor adapted in any way, this is considered reasonable agreement with the observations, especially as the inner disk ratio is decreasing with time while the outer disk ratio is increasing with time. At a time of 2 Myr, the peak ratio in the inner region is  $\sim 0.7$  while the peak outer ratio is  $\sim 0.6$ . Compared to the observed values, which are shown as gray shaded regions in the bottom-left panel of Figure 6, the resultant peak values in the inner region are of the same order of magnitude at 1 Myr but a factor of 20 underestimated at 2 Myr. Meanwhile, the peak ratio in the outer region is more consistent across the different times of extraction and within a

factor of 2 of the observations. The radial behavior of the ice-phase column density ratio shows a similar shape and trend with an overall decrease throughout the inner region and a peak colocated with the outer dust ring. That the ice- and gas-phase ratios are similar shows that we are likely primarily tracing the desorption of ices in our observations, as well as that the main desorption mechanisms are those suggested by the model: thermal desorption in the inner region and photodesorption in the outer region. The agreement with the cometary ratio in the inner region (see Figure 5) strongly supports that we are seeing “fresh” ice sublimation here. It should be noted, however, that the column density and column density ratio plots in Appendix G (Figure 14), which are not radially binned, show peaks within the inner component that are averaged out in our observations and the radially binned model.

HD 100546 is also one of the few disks within which cold water was detected with Herschel (L. M. Pirovano et al. 2022). The fractional abundance of cold water emission from the outer disk was estimated using a forward model to be  $3 \times 10^{-9}$  in the region where photodesorption is expected to be the chemical origin. The peak fractional abundance of  $\text{CH}_3\text{OH}$  predicted by the model here in the same region and at a time of 1 Myr is a few times  $10^{-11}$  (see Figure 15); however, this model does underpredict the column density in the outer ring by around a factor of 10. This implies a peak fractional abundance of  $\text{CH}_3\text{OH}$  closer to a few times  $10^{-10}$ , leading to a  $\text{CH}_3\text{OH}/\text{H}_2\text{O}$  gas-phase abundance ratio of order 0.1 (10%). This estimation lies at the higher end of the ratio of  $\text{CH}_3\text{OH}/\text{H}_2\text{O}$  seen in comets (typically of order 0.1%–10%; see, e.g., D. Bockelée-Morvan & N. Biver 2017). That the gas-phase abundance is estimated to be close to the higher end of the observed ratio for cometary ice suggests that we could be directly probing the composition of the ice reservoir in the outer ring, despite the origin being photodesorption. However, as previously mentioned, experiments have suggested that the efficiency of intact  $\text{CH}_3\text{OH}$  photodesorption is around 100–1000 lower than that of  $\text{H}_2\text{O}$ , which would suggest a gas-phase  $\text{CH}_3\text{OH}/\text{H}_2\text{O}$  of no higher than  $\sim 0.001$  (0.1%) assuming an ice-phase ratio as high as 0.1 (10%; K. I. Öberg et al. 2009; M. Bertin et al. 2016). Indeed, the model results for gas-phase  $\text{H}_2\text{O}$  show a higher fractional abundance and greater radial and vertical extent than that for gas-phase  $\text{CH}_3\text{OH}$ , reflecting the different photodesorption efficiencies for both species (not shown here).

There are multiple possible explanations for this apparent discrepancy. Either  $\text{CH}_3\text{OH}$  is able to be synthesized efficiently in the colder outer regions, thereby increasing the  $\text{CH}_3\text{OH}/\text{H}_2\text{O}$  ice (or gas) ratio to values higher than the cometary value, or there is another nonthermal desorption mechanism dominating the gas-phase abundances, which has similar efficiencies for both  $\text{CH}_3\text{OH}$  and  $\text{H}_2\text{O}$ , e.g., chemical or reactive desorption. Future gas-grain astrochemical models tailored to the dust and gas structure of HD 100546 are needed to test these theories.

## 7. Conclusions

In this work, we analyzed emission from multiple rotational transitions of  $\text{CH}_3\text{OH}$  and  $\text{H}_2\text{CO}$  arising from the structured disk around the Herbig Ae star HD 100546 as observed with ALMA. Our aim was to measure the rotational temperature and column density of each molecule and ascertain its chemical origin. The main conclusions of this paper can be summarized as follows:

1. We detect the organic molecules  $\text{H}_2\text{CO}$  (three ortho and two para transitions) and  $\text{CH}_3\text{OH}$  (10 transitions). Both molecules have a centrally concentrated component within 110 au of the star and a ring of molecular emission centered at 220 au, which is associated with a faint ring of millimeter dust.
2. Using a rotational diagram, we find that  $\text{CH}_3\text{OH}$  decreases in column density from the inner ( $1.4_{-0.3}^{+0.4} \times 10^{14} \text{ cm}^{-2}$ ) to the outer ( $1.2_{-0.1}^{+0.1} \times 10^{13} \text{ cm}^{-2}$ ) region, whereas the column density of  $\text{H}_2\text{CO}$  is constant across the two emission components at approximately  $9 \times 10^{12} \text{ cm}^{-2}$ .
3. The  $\text{CH}_3\text{OH}/\text{H}_2\text{CO}$  ratio varies from  $14.6_{-4.6}^{+5.2}$  in the inner disk to  $1.3_{-0.2}^{+0.3}$  in the outer disk. This could be due to a contribution of gas-phase formation of  $\text{H}_2\text{CO}$  in the outer disk, or that there is a higher abundance of  $\text{CH}_3\text{OH}$  ice than  $\text{H}_2\text{CO}$  ice in the disk midplane, which is traced in the thermally sublimated reservoir generating the inner component.
4. We find a significant decrease in the rotational temperatures,  $T_{\text{rot}}$ , across the disk for both species.  $T_{\text{rot}}$  for  $\text{CH}_3\text{OH}$  has values of  $152_{-27}^{+35} \text{ K}$  and  $52_{-6}^{+8} \text{ K}$  in the inner and outer disk, respectively, whereas the equivalent values for  $\text{H}_2\text{CO}$  are  $76_{-8}^{+9} \text{ K}$  and  $31_{-2}^{+2} \text{ K}$ . The values for the inner disk are consistent with the inner component arising from thermal desorption of ices at each species' respective snowline or snow surface, whereas those for the outer disk are consistent with a nonthermal desorption origin (with gas-phase formation also possibly contributing to the  $\text{H}_2\text{CO}$  abundance here). The coincidence of the  $\text{CH}_3\text{OH}$  and  $\text{H}_2\text{CO}$  outer components of emission with the faint millimeter dust ring suggests that the dust grains sculpted into this ring are icy.
5. The higher temperature seen in the inner region of HD 100546 is comparable to temperatures seen toward younger objects, suggesting a similar chemical origin (i.e., thermal desorption from the ice phase). However,  $\text{CH}_3\text{OH}$  in the outer region of HD 100546 has a more similar rotational temperature to that for the disk around TW Hya, where photodesorption is the most probable chemical origin of gas-phase  $\text{CH}_3\text{OH}$ . We also note that a similar trend in  $\text{CH}_3\text{OH}/\text{H}_2\text{CO}$  ratio across the HD 100546 disk has been seen for the disk around the Herbig Ae star, HD 169142.
6. Comparing our results with predictions from a chemical model of the HD 100546 disk, we find that the model results are consistent with the observed radial column density trends in  $\text{CH}_3\text{OH}$  and  $\text{H}_2\text{CO}$ , in that both decrease going from the inner to outer regions. The model predicts a steeper decrease in the column density of  $\text{CH}_3\text{OH}$  compared with that for  $\text{H}_2\text{CO}$ , which is also consistent with the observations. The peak column density ratio ( $\text{CH}_3\text{OH}/\text{H}_2\text{CO}$ ) in the inner region predicted at 1 Myr is of the same order of magnitude as that seen in the observations, while the peak value predicted at 2 Myr is approximately 1–2 orders of magnitude lower.

The original detection of gas-phase methanol in the disk around HD 100546 was serendipitous and led to the conclusion that a significant fraction of the ice reservoir is inherited from an earlier evolutionary phase (A. S. Booth et al. 2021). Our results support this notion, as they suggest that we are seeing “fresh” ice sublimation in this disk as shown by the similar  $\text{CH}_3\text{OH}/\text{H}_2\text{CO}$  ratio seen in HD 100546 to that seen in solar

system comets. However, since the original detection of  $\text{CH}_3\text{OH}$  in HD 100546, it has also been detected in the Herbig disks around HD 169142 (A. S. Booth et al. 2023b) and IRS 48 (N. van der Marel et al. 2021). Given the lack of gas-phase  $\text{CH}_3\text{OH}$  detected toward the Herbig disks, MWC 480 and HD 163296 (R. A. Loomis et al. 2018; M. T. Carney et al. 2019; Y. Yamato et al. 2024), there is an apparent chemical diversity among Herbig objects that is likely related to their structure: the disks where gas-phase  $\text{CH}_3\text{OH}$  is detected all possess inner cavities that allow for direct irradiation of the icy midplane, thus revealing the ice composition. These class of disks are now providing valuable insight into the composition of the ice reservoir, which still remains elusive to observe in colder disks, including in the disks around T Tauri stars. The results reported here for HD 100546 show that the building blocks of prebiotic molecules (e.g.,  $\text{CH}_3\text{OH}$ ) are present during the epoch of planet formation. However, further high-sensitivity and potentially longer-wavelength observations of COMs targeting multiple Herbig disks are required in order to determine if this conclusion is generally applicable.

### Acknowledgments

We thank Ewine van Dishoeck for useful feedback on a draft of this manuscript. L.E. acknowledges financial support from the Science and Technology Facilities Council (grant No. ST/X001016/1). A.S.B. is supported by a Clay Postdoctoral Fellowship from the Smithsonian Astrophysical Observatory. C.W. acknowledges financial support from the Science and Technology Facilities Council and UK Research and Innovation (grant Nos. ST/X001016/1 and MR/T040726/1). J.D.I. acknowledges support from an STFC Ernest Rutherford Fellowship (ST/W004119/1) and a University Academic Fellowship from the University of Leeds. L. Keyte is funded by UKRI guaranteed funding for a Horizon Europe ERC consolidator grant (EP/Y024710/1) Support for C. J. Law was provided by NASA through the NASA Hubble Fellowship grant No. HST-HF2- 51535.001-A awarded by the Space Telescope Science Institute, which is operated by the Association of Universities for Research in Astronomy, Inc., for NASA, under contract NAS5-26555. S.N. is grateful for support from Grants-in-Aid for JSPS (Japan Society for the Promotion of Science) Fellows grant Nos. JP23KJ0329 and MEXT/JSPS Grants-in-Aid for Scientific Research (KAKENHI) grant Nos. JP20H05845, JP20H05847, JP23K13155, and JP24K00674. M.T. acknowledges support from the ERC grant 101019751 MOLDISK. M.L. is funded by the European Union (ERC, UNVEIL, 101076613). Views and opinions expressed are, however, those of the author(s) only and do not necessarily reflect those of the European Union or the European Research Council. Neither the European Union nor the granting authority can be held responsible for them. This paper makes use of the following ALMA data: 2019.1.00193.S and 2021.1.00738.S. ALMA is a partnership of ESO (representing its member states), NSF (USA) and NINS (Japan), together with NRC (Canada), NSC and ASIAA (Taiwan), and KASI (Republic of Korea), in cooperation with the Republic of Chile. The Joint ALMA Observatory is operated by ESO, AUI/NRAO, and NAOJ. The data used are publicly available on the ALMA Archive (<https://almascience.nrao.edu/aq/>) with project codes 2019.1.00193.S and 2021.1.00738.S. The model used is available on request from C. Walsh. The data products, images, spectra, and modeling results are available on request from L. Evans.



## Appendix A

### Moment 0 Maps

Figure 7 shows the moment 0 maps for all 10  $\text{CH}_3\text{OH}$  lines used in our analysis.

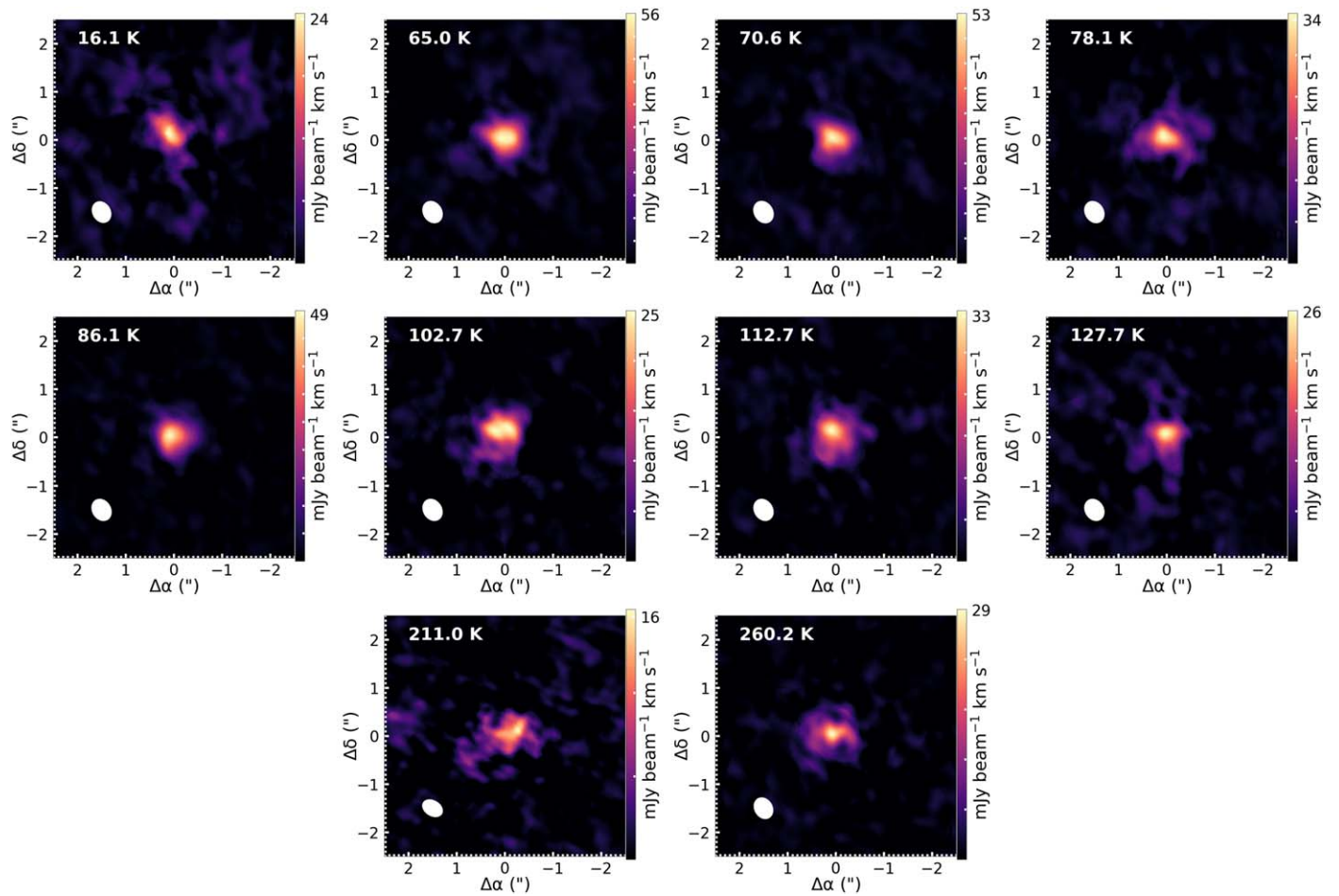


**Figure 7.** Moment 0 maps for all 10 Cycle 8  $\text{CH}_3\text{OH}$  transitions used in the flux extraction and rotational diagram analysis, in ascending order of  $E_u$ . The synthesized beam is represented by the white ellipse in the bottom-left corner.

## Appendix B

### Radial Profiles

Figure 8 shows the azimuthally averaged radial profiles for all of the Cycle 8 transitions of  $\text{CH}_3\text{OH}$ .

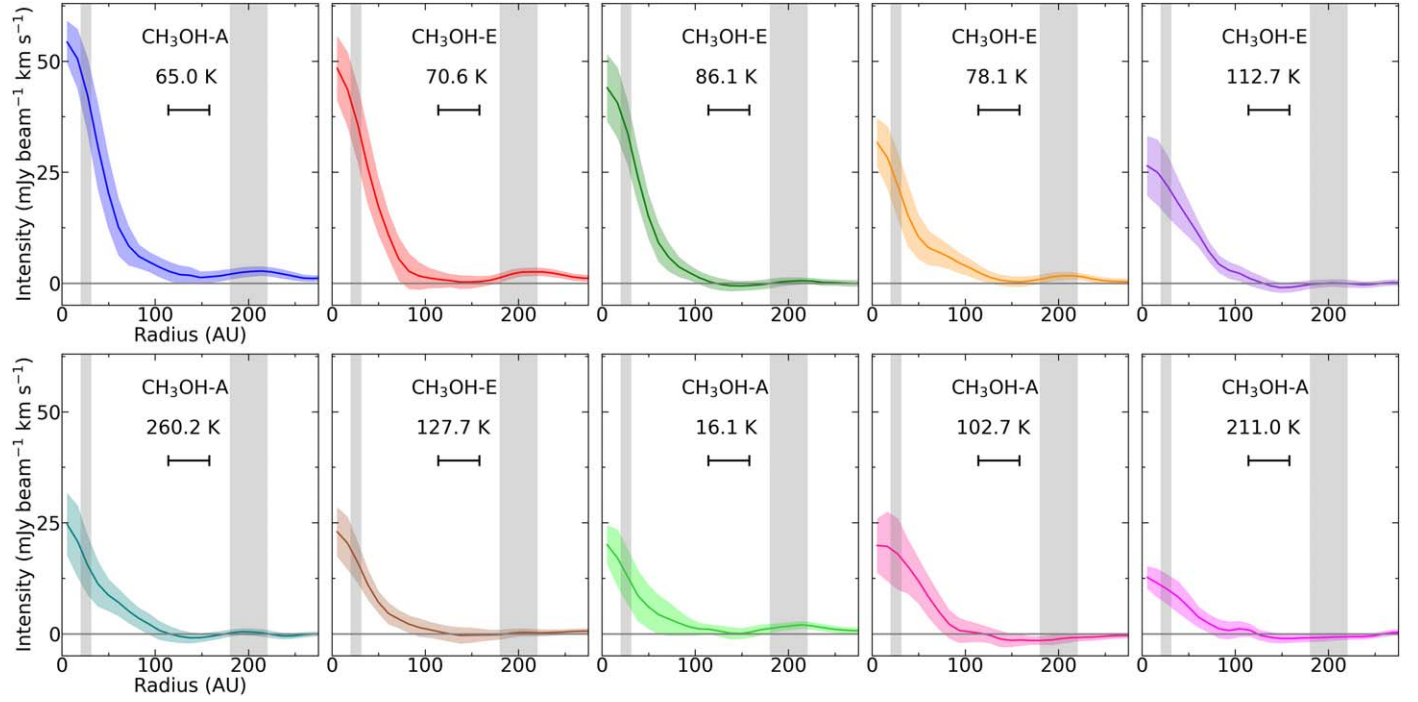


**Figure 8.** Azimuthally averaged radial profiles for all of the Cycle 8 transitions of  $\text{CH}_3\text{OH}$  along with associated error bars in order of decreasing peak intensity. The radial ranges of the peaks of the two dust rings seen in the 0.9 mm continuum emission between  $\sim 20$ – $31$  au and  $\sim 180$ – $220$  au are denoted by the gray shaded regions. The horizontal bars show the FWHM of the synthesized beam.

### Appendix C Spectra

Figures 9 and 10 show the  $\text{H}_2\text{CO}$  spectral lines extracted using *gofish* between radial ranges of 0–110 au and between 180–260 au, respectively.

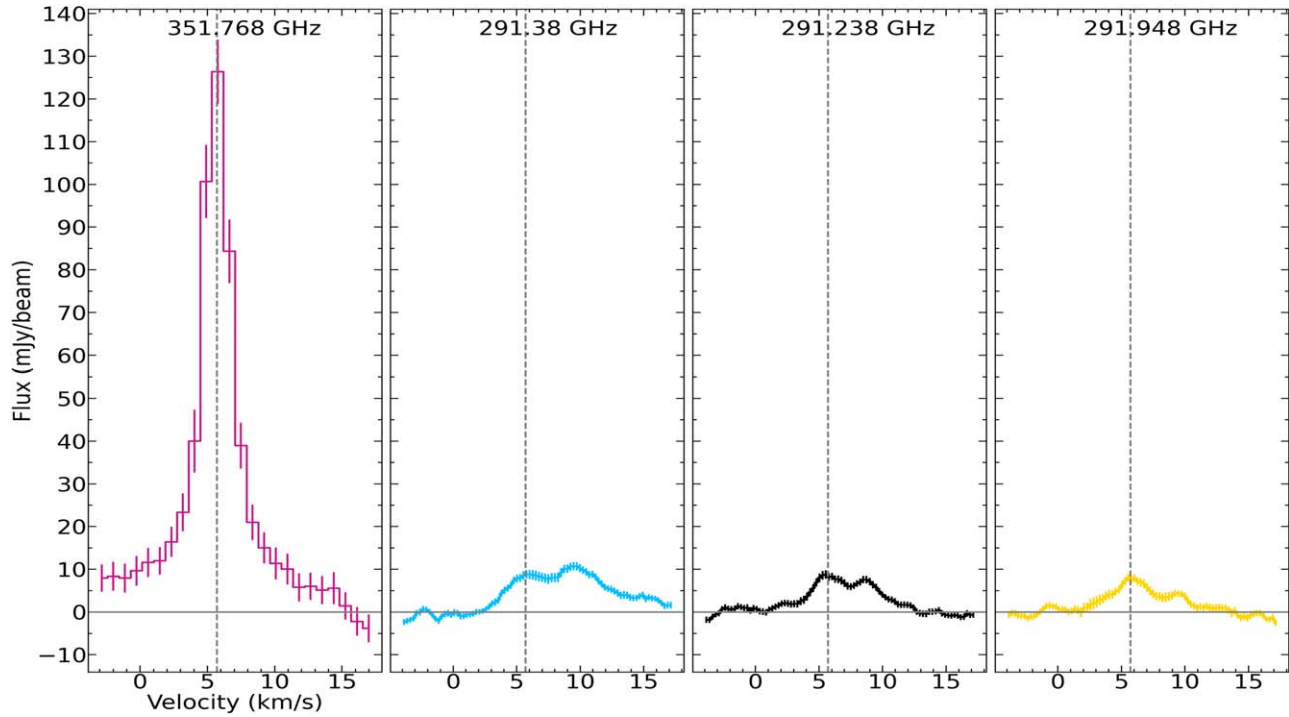


**Figure 9.**  $\text{H}_2\text{CO}$  spectral lines extracted using *gofish* within 110 au for the full velocity range of the spw ( $-4.2$  to  $17.4 \text{ km s}^{-1}$ ). The gray dashed line indicates the source velocity at  $5.7 \text{ km s}^{-1}$ .

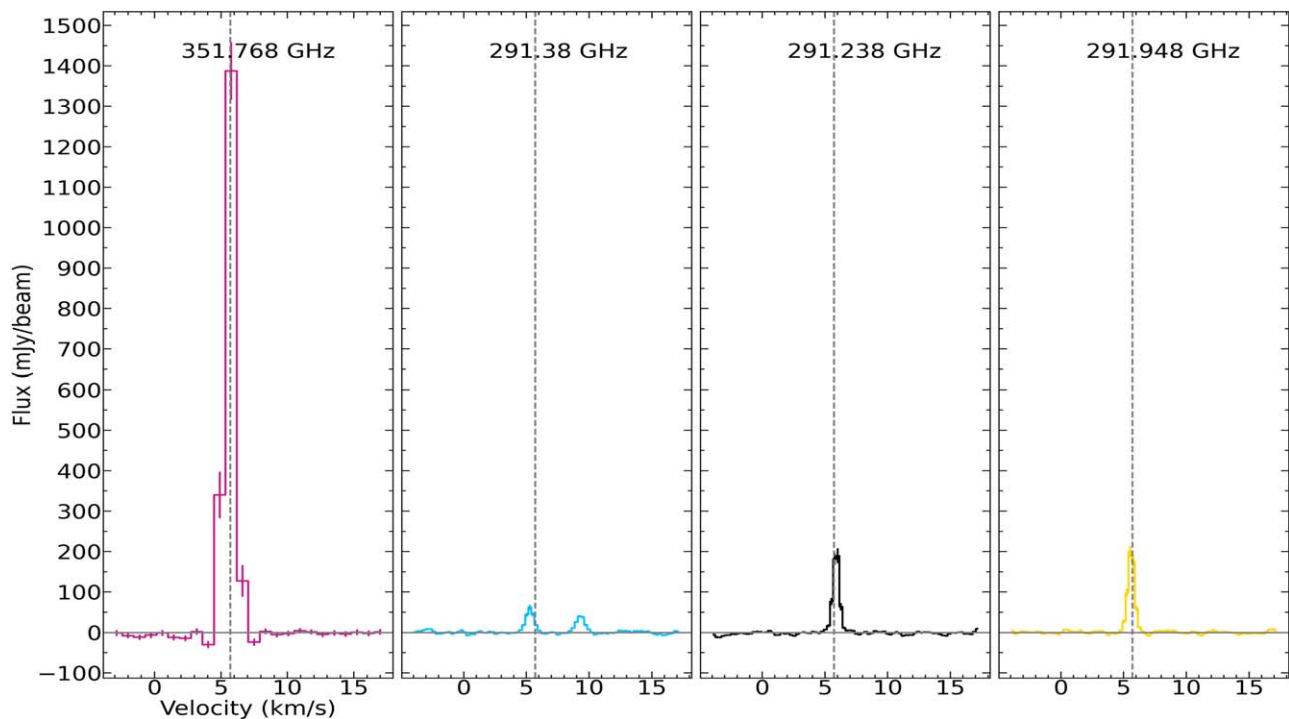


**Figure 10.**  $\text{H}_2\text{CO}$  spectral lines extracted using *gofish* between 180 and 260 au for the full velocity range of the spw ( $-4.2$  to  $17.4 \text{ km s}^{-1}$ ). The gray dashed line indicates the source velocity at  $5.7 \text{ km s}^{-1}$ .



### Appendix D

#### Corner Plots

Figure 11 shows the corner plots generated from the MCMC best fits used to produce the rotational diagrams shown in Figure 4.

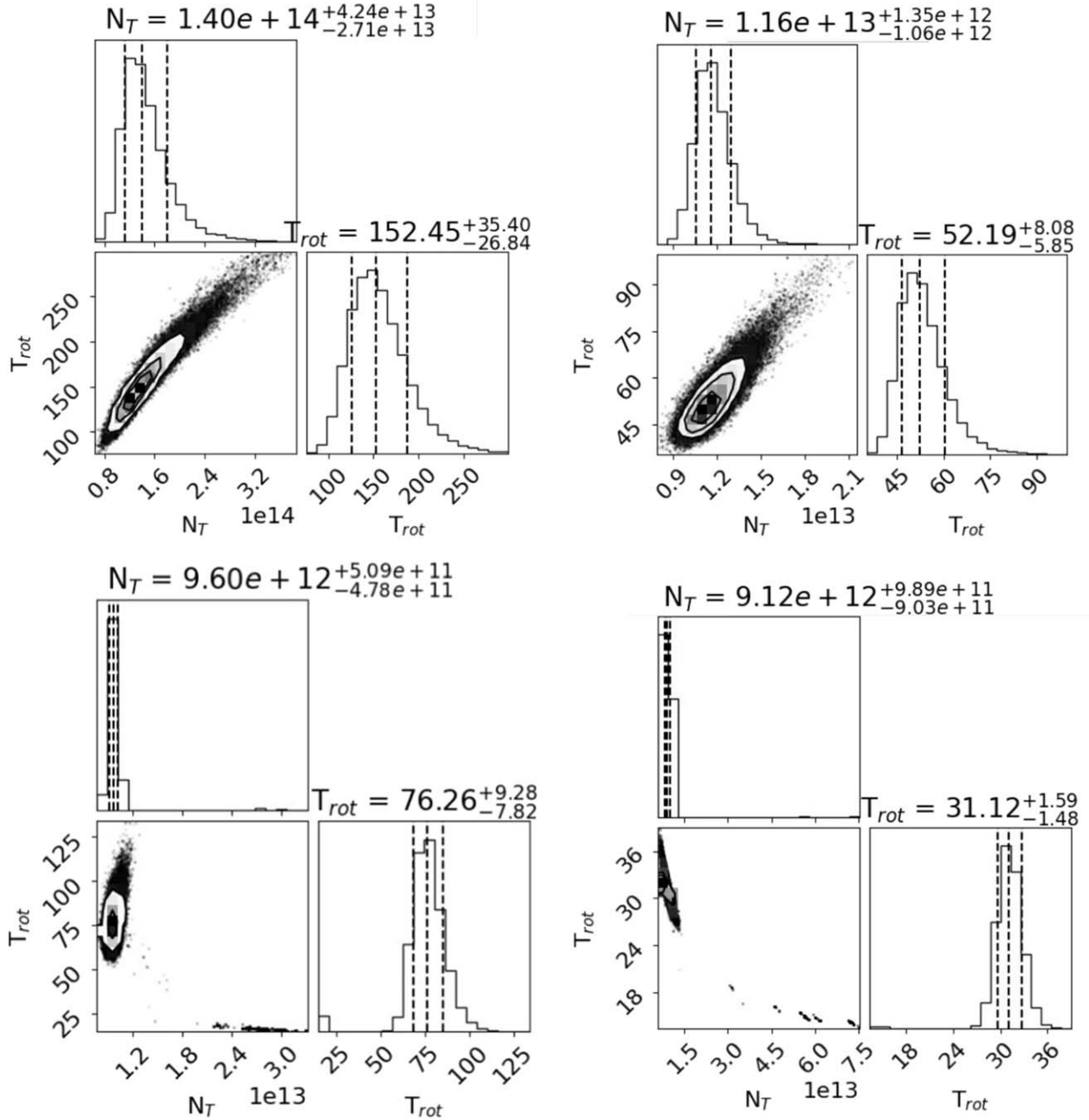


**Figure 11.** Corner plots generated from the MCMC best fits used to produce the rotational diagrams shown in Figure 4. Clockwise from top left: CH<sub>3</sub>OH inner component, CH<sub>3</sub>OH outer component, H<sub>2</sub>CO outer component, H<sub>2</sub>CO inner component.

### Appendix E Desorption Temperature Calculation

Here we detail the methodology used to calculate the desorption temperatures of  $\text{CH}_3\text{OH}$  and  $\text{H}_2\text{CO}$  in the midplane of HD 100546. The rate of desorption ( $k_d$ ) per second from dust grains can be calculated using Equation (E1) (T. I. Hasegawa et al. 1992),

$$k_d = \nu_0 \exp\left(-\frac{E_d}{T_d}\right). \quad (\text{E1})$$

In Equation (E1),  $E_d$  represents the binding energy of the species,  $T_d$  represents the dust grain temperature, both in kelvin, while  $\nu_0$ , the characteristic vibrational frequency of the adsorbed species in its potential well, is given by

$$\nu_0 = \sqrt{\frac{2n_s E_d}{\pi^2 m}}, \quad (\text{E2})$$

where  $n_s$  is the number density of surface sites on each dust grain ( $\text{cm}^{-2}$ ),  $E_d$  is the binding energy (erg), while  $m$  is the mass of the species (g). We assume that the binding energies of  $\text{CH}_3\text{OH}$  and  $\text{H}_2\text{CO}$  are 3820 K and 3260 K, respectively, as recommended in E. M. Penteadó et al. (2017) using data from M. P. Collings et al. (2004) and J. A. Noble et al. (2012). Meanwhile, the rate of freeze-out per second is given by

$$k_f = \langle v \rangle \sigma_d n_d S, \quad (\text{E3})$$

where  $\sigma_d$  is the cross-sectional area ( $\text{cm}^2$ ) of a dust grain with radius  $a$  (hence,  $\sigma = \pi a^2$ ),  $n_d$  is the number density of the dust grains ( $\text{cm}^{-3}$ ),  $S$  is the sticking coefficient (for this case, it is safe to assume a value of  $S = 1$  for both species) while  $\langle v \rangle$  is the thermal velocity ( $\text{cm s}^{-1}$ ) of the species of mass  $m$  (g) and at gas temperature  $T_g$  (K) and is given by

$$\langle v \rangle = \sqrt{\frac{8k_B T_g}{\pi m}}, \quad (\text{E4})$$

where  $k_B$  is the Boltzmann constant in cgs units. We assume a range of values for the density of the gas in the midplane,  $n_{\text{gas}}$ , between  $10^{10}$  and  $10^{12} \text{ cm}^{-3}$  (M. Kama et al. 2016). Using the assumed fractional abundance of dust grains of  $1.3 \times 10^{-12}$ , we therefore obtain a range of values for  $k_f$ . In order to obtain the desorption temperature, we assume that  $k_d = k_f$ , as approximately equal quantities of the species will be in the gas and ice phases (M. L. R. van't Hoff et al. 2017). In order to obtain  $T_{\text{des}}$ , we therefore plot  $k_d(T)$  and  $k_f(T)$  on a single axis (see Figure 12) and obtain the range of values for  $T_{\text{des}}$  as the temperature values where  $k_d$  intercepts the multiple  $k_f$  curves (according to our assumed values of  $n_{\text{gas}}$ ).

According to Figure 12, using the recommended binding energy for  $\text{CH}_3\text{OH}$  (3820 K; M. P. Collings et al. 2004) leads to a higher range of desorption temperatures from 96–109 K, depending on the gas density. Meanwhile,  $\text{H}_2\text{CO}$  would desorb at temperatures ranging from 82–93 K (M. P. Collings et al. 2004; J. A. Noble et al. 2012; E. M. Penteadó et al. 2017).

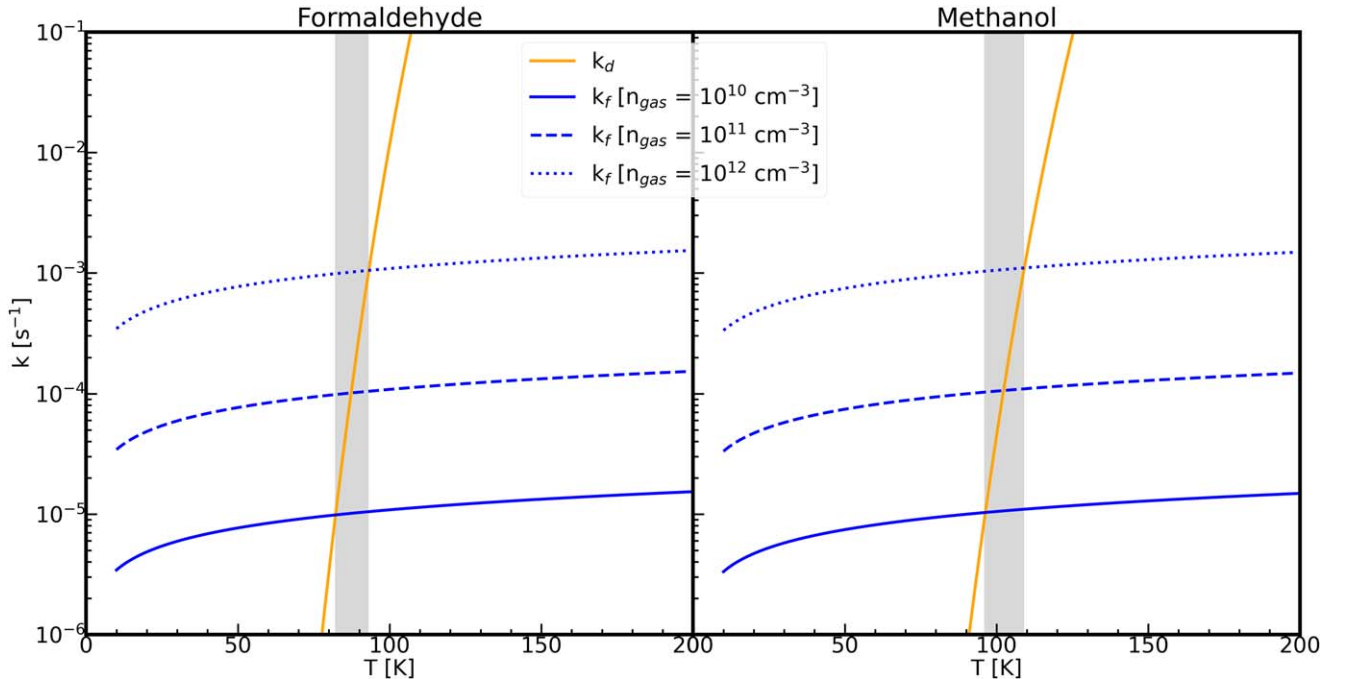


**Figure 12.** Plot showing the rate of desorption (orange) and gas density-dependent rates of freeze-out (blue) for  $\text{H}_2\text{CO}$  (left panel) and  $\text{CH}_3\text{OH}$  (right panel); the  $x$ -values of the intersections are equal to the desorption temperatures.

## Appendix F

### Rotational Temperature Discussion

Cold methanol has been detected as early as the prestellar stage, with a rotational temperature of  $5.3^{+2.2}_{-1.1}$  K measured toward L1544 (A. Punanova et al. 2018). Values toward Class 0 objects vary greatly according to the literature, with values greater than 300 K measured toward embedded protostars in Perseus (Y.-L. Yang et al. 2021) and values as low as 11 K measured toward deeply embedded protostars in other clouds (D. M. Graninger et al. 2016). Generally speaking, however, the Class 0 measurements are higher than those measured toward L1544 and fall in line with the majority of measured values toward Class 0/I and I objects, which tend to lie in the approximate range of 100–300 K. There are also outliers in these slightly more evolved objects, however. For example, B. Riaz et al. (2023) measured a sample of 14 Class 0/I proto-brown dwarfs (PBDs) and found that, while a cold emission component with an average  $T_{\text{rot}}$  of 5–7 K exists in all of them, 78% of the sample also exhibited a warmer component with an average measured  $T_{\text{rot}}$  of 17–28 K. Both of these measurements, however, are lower than those generally found among other Class 0/I objects according to Figure 13. Similarly, D. M. Graninger et al. (2016) measured a relatively low  $T_{\text{rot}}$  value of 13 K toward both of the Class I sources B1-a and B5 IRS1. There is, therefore, perhaps some dependence of  $T_{\text{rot}}$  on the nascent cloud and/or the size of the object. It should further be noted that some of the observations presented in Table 4, whether due to being single-dish or otherwise, fail to resolve the innermost regions in which thermal desorption is occurring. Meanwhile, a lower  $T_{\text{rot}}$  value of  $35.8^{+25.1}_{-10.3}$  K has recently been measured toward the T Tauri object

TW Hya (J. D. Ilee et al. 2025, in preparation), while a value of  $103^{+6}_{-5}$  K was measured toward the Herbig object IRS 48 (N. van der Marel et al. 2021); intriguingly, this is lower than the value for  $T_{\text{rot}}$  measured in  $\text{H}_2\text{CO}$  toward this disk, which is the opposite trend to that seen in HD 100546. This trend in IRS 48 has been corroborated by M. Temmink et al. (2025), although there is large scatter in these results due to the non-negligible effects of subthermal excitation.

As illustrated in Figure 13, our results for the inner region of HD 100546 are consistent with the hot component of emission from the majority of the Class 0, 0/I, and I objects. Hot core/corino emission is also thought to arise from thermal desorption of ices on grain mantles when the surrounding core is heated to temperatures  $\gtrsim 100$  K (see, e.g., J. K. Jørgensen et al. 2020). The rotational temperature of  $\text{CH}_3\text{OH}$  in the outer region of HD 100546 is more consistent with that measured for the disk around the T Tauri star, TW Hya. The disk around TW Hya is colder than that around HD 100546, with disk models fitted to the observations suggesting the absence of a CO snowline in the disk around HD 100546 (M. Kama et al. 2016). Models have predicted a small amount of CO freeze-out in the dust ring of HD 100546 (a factor of  $\sim 10$ –100 depletion); however, this is not predicted to contribute significantly to the production of  $\text{CH}_3\text{OH}$  due to the low dust mass of this source (M. Leemker et al. 2024). However, the similar  $T_{\text{rot}}$  for  $\text{CH}_3\text{OH}$  for the disk-integrated emission around TW Hya and the outer component of emission in HD 100546 indicates a common chemical origin for gas-phase methanol that is likely driven by nonthermal desorption from icy grains.

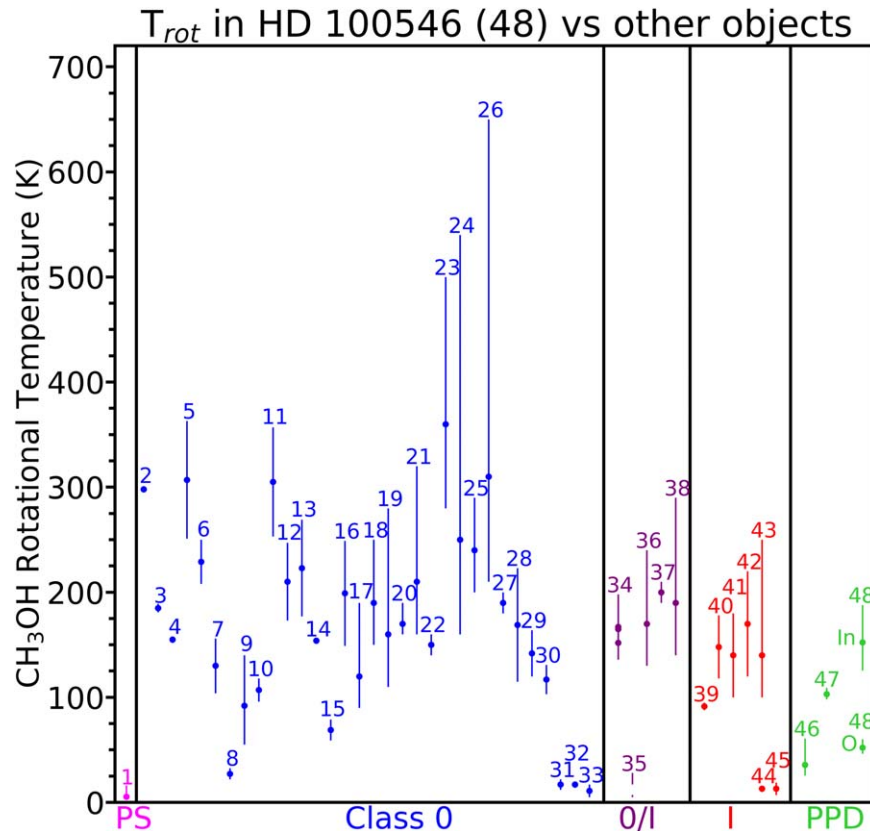


**Figure 13.**  $T_{\text{rot}}$  values for  $\text{CH}_3\text{OH}$  measured toward the inner and outer regions of HD 100546 compared to values measured toward objects of varying evolutionary stages. Numbers have been used to denote each object; please refer to Appendix G (Table 4) for the object and reference(s) associated with each number. Note that “PS” represents prestellar core values while “PPD” represents those of protoplanetary disks (both T Tauri and Herbig). Separate  $T_{\text{rot}}$  measurements toward the inner and outer emission components of HD 100546 (48) are denoted “In” and “O,” respectively.



**Table 4**  
Associated Letter and/or Number along with Reference(s) to Each Object in Figures 5 and 13

Stage	Name	Number	Letter	References
Prestellar	L1544	1	...	A. Punanova et al. (2018)
Class 0	G208.68-19.20N1	2	...	S.-Y. Hsu et al. (2020)
	G211.47-19.27S	3	...	S.-Y. Hsu et al. (2020)
	G210.49-19.79W	4	...	S.-Y. Hsu et al. (2020)
	IRAS 4A2	5	A	A. Belloche et al. (2020), V. Taquet et al. (2015)
	IRAS 2A1	6	B	A. Belloche et al. (2020), V. Taquet et al. (2015)
	IRAS 16293-A	7	C	J. K. Jørgensen et al. (2020), M. V. Persson et al. (2018), S. Manigand et al. (2020)
	IRAS 16293-B	...	D	J. K. Jørgensen et al. (2020), M. V. Persson et al. (2018), S. Manigand et al. (2020)
	Cep E-mm	8	E	J. Ospina-Zamudio et al. (2018)
	HH 212	9	F	C.-F. Lee et al. (2022)
	Orion B9-SMM3	...	G	O. Miettinen (2016)
	L1448-C	10	...	A. Belloche et al. (2020)
	IRAS 4B	11	...	A. Belloche et al. (2020)
	SerpM-S68N	12	...	A. Belloche et al. (2020)
	SerpM-SMM4B	13	...	A. Belloche et al. (2020)
	SerpS-MM18a	14	...	A. Belloche et al. (2020)
	SerpS-MM18b	15	...	A. Belloche et al. (2020)
	L1157	16	...	A. Belloche et al. (2020)
	Per-emb 26	17	...	Y.-L. Yang et al. (2021)
	Per-emb 22A	18	...	Y.-L. Yang et al. (2021)
	Per-emb 22B	19	...	Y.-L. Yang et al. (2021)
	Per-emb 12B	20	...	Y.-L. Yang et al. (2021)
	Per-emb 13	21	...	Y.-L. Yang et al. (2021)
	Per-emb 21	22	...	Y.-L. Yang et al. (2021)
	Per-emb 18	23	...	Y.-L. Yang et al. (2021)
	B1-bs	24	...	Y.-L. Yang et al. (2021)
	Per-emb 11A	25	...	Y.-L. Yang et al. (2021)
	Per-emb 11C	26	...	Y.-L. Yang et al. (2021)
	Per-emb 29	27	...	Y.-L. Yang et al. (2021)
	FIR6c-a	28	...	M. Bouvier et al. (2022)
	MMS9-a	29	...	M. Bouvier et al. (2022)
	MMS5	30	...	M. Bouvier et al. (2022)
	B1-c	31	...	D. M. Graninger et al. (2016)
	IRAS 03245+3002	32	...	D. M. Graninger et al. (2016)
	L1014 IRS	33	...	D. M. Graninger et al. (2016)
Class 0/I	BHB 07-11	34 <sup>a</sup>	...	C. Vastel et al. (2022)
	14 Proto-brown dwarfs	35 <sup>b</sup>	...	B. Riaz et al. (2023)
	Per-emb 20	36	...	Y.-L. Yang et al. (2021)
	Per-emb 44	37	...	Y.-L. Yang et al. (2021)
	Per-emb 27	38	...	Y.-L. Yang et al. (2021)
Class I	V883 Ori	39	...	M. L. R. van't Hoff et al. (2018), J.-E. Lee et al. (2019)
	L1551-IRS5	40	...	S. Mercimek et al. (2022)
	SVS13-A VLA4A	41	...	E. Bianchi et al. (2022)
	SVS13-A VLA4B	42	...	E. Bianchi et al. (2022)
	Per-emb 35A	43	...	Y.-L. Yang et al. (2021)
	B1-a	44	...	D. M. Graninger et al. (2016)
	B5 IRS1	45	...	D. M. Graninger et al. (2016)
	DG Tau B	...	H	A. Garufi et al. (2020)
	HL Tau	...	J	A. Garufi et al. (2022)
	IRAS 040302+2247	...	K	L. Podio et al. (2020)
T Tauri	TW Hya	46	L	J. D. Ilee et al. (2025, in preparation).
	DG Tauri	...	M	L. Podio et al. (2019)
Herbig	HD 169142	...	N <sup>c</sup>	A. S. Booth et al. (2023b)
	HD 163296	...	O	M. T. Carney et al. (2019)
	IRS 48	47	P	N. van der Marel et al. (2021), A. S. Booth et al. (2024b), M. Temmink et al. (2025)
	HD 100546	48 <sup>c</sup>	Q <sup>c</sup>	This work

**Notes.**

<sup>a</sup>  $T_{\text{rot}}$  values are measured for three emission components, each represented with a separate point in Figure 13.

<sup>b</sup> Two  $T_{\text{rot}}$  values were measured; these are both shown in Figure 13 as average values over the PBDs in which each component appears.

<sup>c</sup> Separate values are measured toward inner and outer components.

## Appendix G

### Chemical Modeling

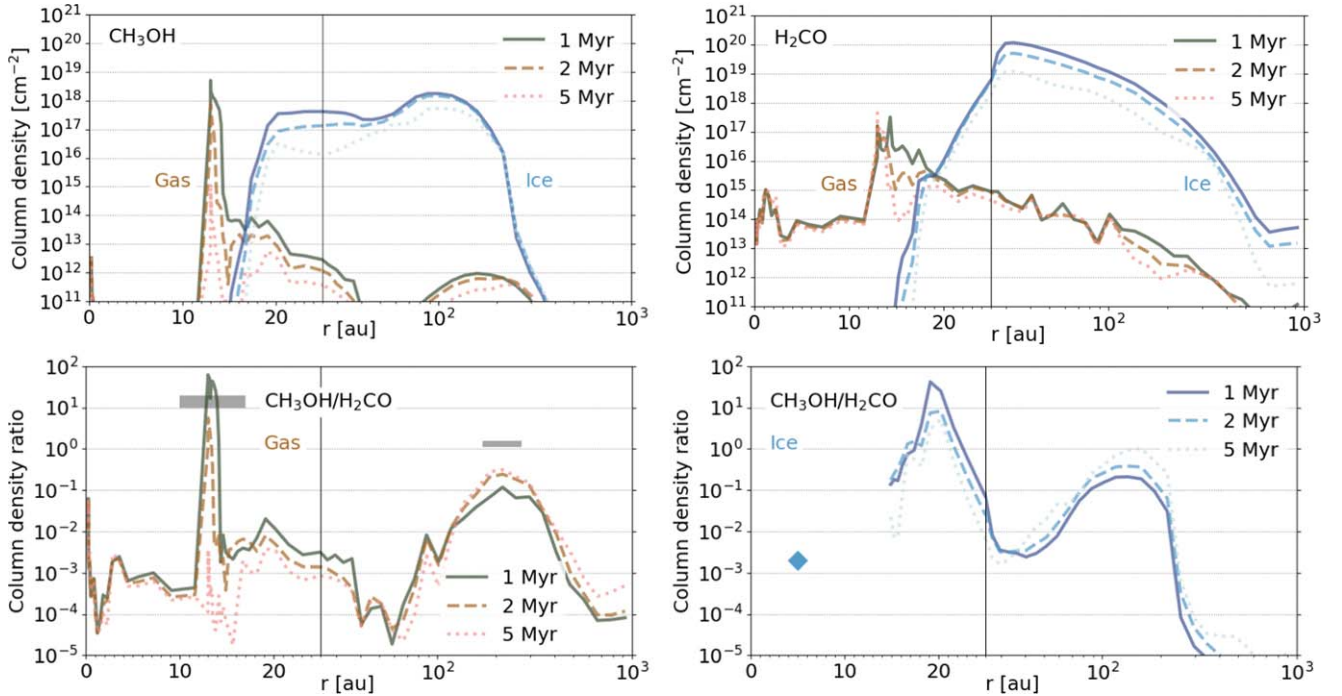
The gas-grain chemical model utilized to supplement our results couples a 2D physical abundance model for HD 100546, first published in M. Kama et al. (2016), with a reaction network based on the UMIST Database for Astrochemistry (D. McElroy et al. 2013), specifically described in C. Walsh et al. (2010, 2012, 2013, 2014, 2015) and first implemented into the code in M. N. Drozdovskaya et al. (2014, 2015). The surface chemistry network for  $\text{CH}_3\text{OH}$  in particular has since been extended (K. J. Chuang et al. 2016), while the chemistry has been updated (refer to C. Walsh et al. 2018) to include fragmentation as a result of nonthermal photodesorption. The photodesorption yield of  $\text{CH}_3\text{OH}$  is  $1.5 \times 10^{-5} \text{ photon}^{-1}$ , which takes into account the fragmentation upon the photodesorption of pure  $\text{CH}_3\text{OH}$  ice (M. Bertin et al. 2016), while the photodesorption yield assumed for  $\text{H}_2\text{CO}$  is  $10^{-3} \text{ photon}^{-1}$ . In total, the reaction network consists of 709 species and 9441 reactions (A. S. Booth et al. 2021). The accretion and desorption rates (A. G. G. M. Tielens & W. Hagen 1982) and the grain-surface reaction rates (T. I. Hasegawa et al. 1992; R. T. Garrod et al. 2008; R. T. Garrod & T. Pauly 2011) are taken from previous literature. The cosmic-ray ionization rate ( $5 \times 10^{-17} \text{ s}^{-1}$ ) along with gas and dust temperature are taken from M. Kama et al. (2016), the gas-to-dust mass ratio is assumed to be 100, while the dust grains are assumed to have a radius of  $0.1 \mu\text{m}$  (A. S. Booth et al. 2021). Initial abundances

Table 5

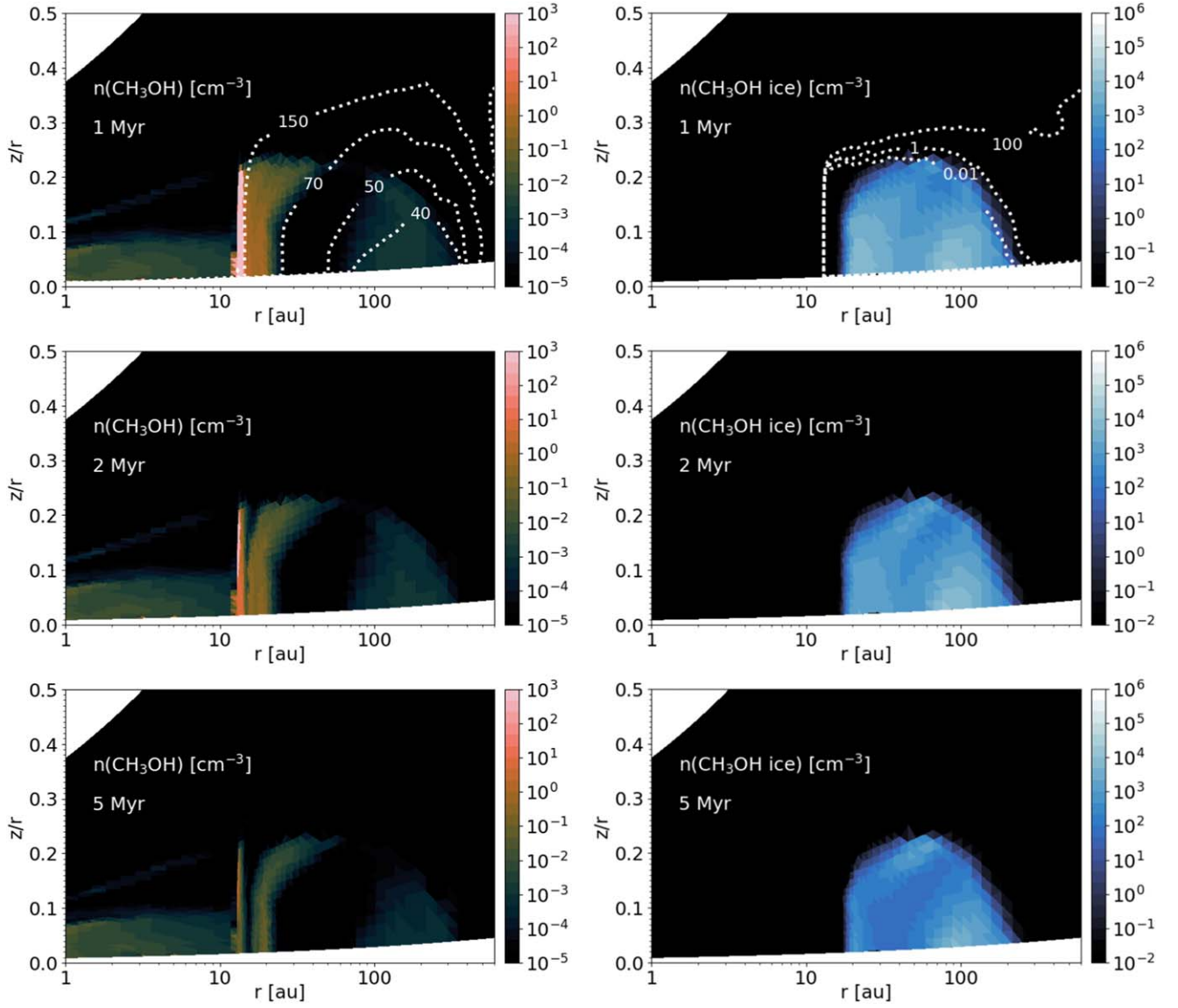
Initial Fractional Abundances of Relevant Species in the Ice Phase Relative to H Nuclei

Species	Initial Fractional Abundance
$\text{CH}_3\text{OH}$	$2.9 \times 10^{-8}$
$\text{H}_2\text{O}$	$1.5 \times 10^{-4}$
$\text{CO}$	$3.6 \times 10^{-5}$
$\text{CO}_2$	$6.7 \times 10^{-7}$
$\text{CH}_4$	$4.2 \times 10^{-6}$
$\text{NH}_3$	$1.4 \times 10^{-6}$

are taken from a single-point dark-cloud chemical model run for 1 Myr from atomic initial conditions, with  $n_{\text{H}} = 2 \times 10^4 \text{ cm}^{-3}$  and cosmic-ray ionization rate  $= 10^{-17} \text{ s}^{-1}$  in order to simulate inheritance of ice from an earlier, colder evolutionary phase. The resultant initial fractional abundances of relevant species in the ice phase relative to H nuclei, as reported in A. S. Booth et al. (2021), are listed in Table 5. We extract the abundances at 1, 2, and 5 Myr and plot the resultant column densities and abundance ratio predictions in Figures 6 (radially binned) and 14 (original). Figures 15 and 16 show the number density of gas and ice phase  $\text{CH}_3\text{OH}$  and  $\text{H}_2\text{CO}$ , respectively, at 1, 2, and 5 Myr as a function of radius ( $r$ ), as well as height divided by radius ( $z/r$ )."



**Figure 14.** Top row: column density calculated as a function of radius for the disk around HD 100546 for  $\text{CH}_3\text{OH}$  (left panel) and  $\text{H}_2\text{CO}$  (right panel) at 1 (solid), 2 (dashed), and 5 (dotted) Myr. Bottom row:  $\text{CH}_3\text{OH}/\text{H}_2\text{CO}$  column density ratio calculated for the gas (left panel) and ice (right panel) phase, at 1 (solid), 2 (dashed), and 5 (dotted) Myr. The brown colors denote gas-phase molecules, while the blue colors represent the ice phase. Note that the  $\text{CH}_3\text{OH}/\text{H}_2\text{CO}$  models plotted for the ice phase (bottom-right panel) are restricted to radii  $\geq 15 \text{ au}$  as the column density in the ice phase is negligible within this radius. The models within 25 au have been plotted on a linear scale to highlight the structure in the inner disk. The gray shaded regions on the bottom-left panel indicate the observed ratios derived in this work for the inner ( $14.6^{+5.2}_{-4.6}$ ) and outer ( $1.3^{+0.3}_{-0.2}$ ) components (note that the radial extent of the shaded regions is arbitrary and is set to guide the eye only). The diamond marker on the bottom-right panel indicates the initial abundance ratio for  $\text{CH}_3\text{OH}/\text{H}_2\text{CO}$  ice adopted in the chemical model ( $2 \times 10^{-3}$ ).







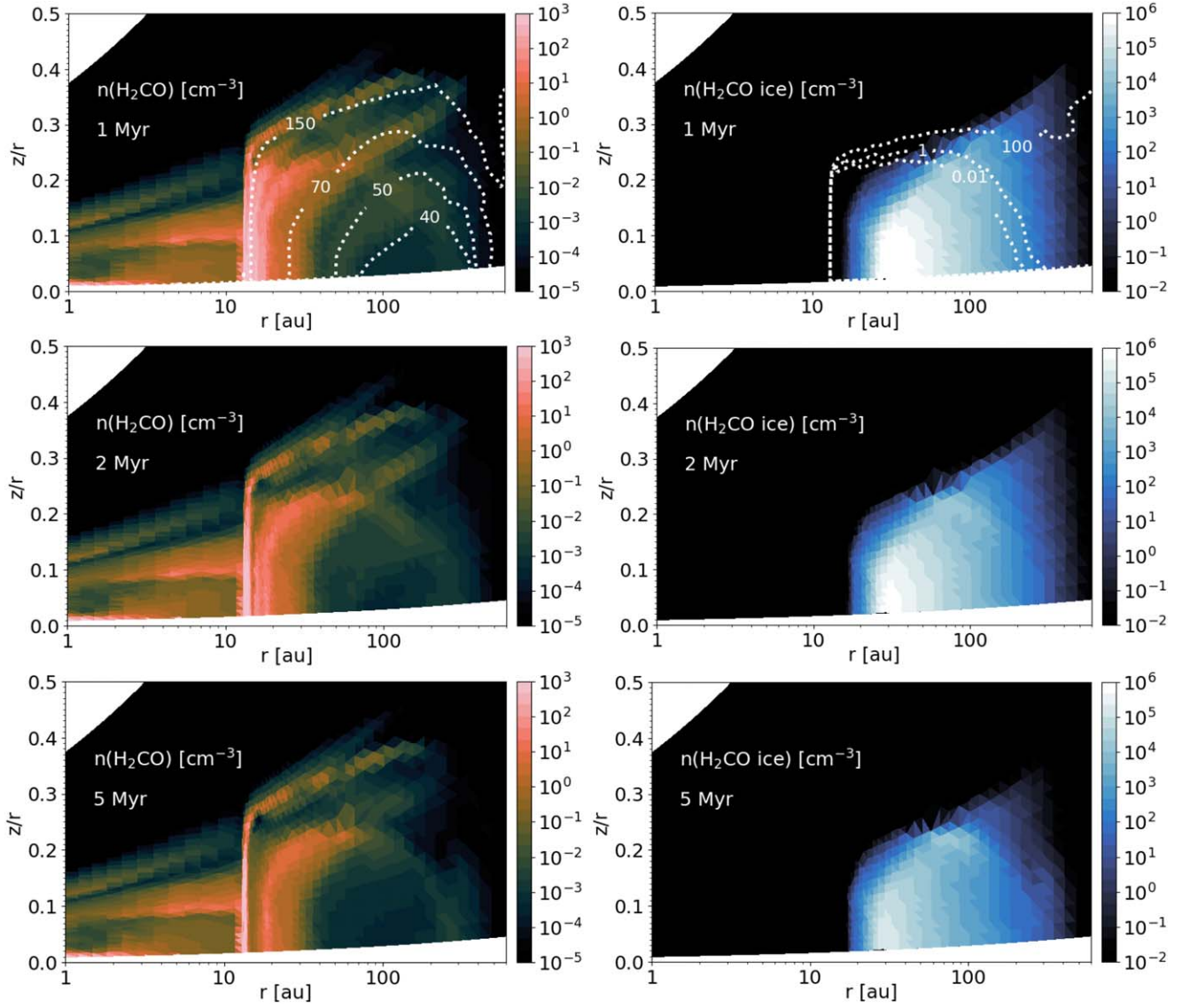







**Figure 15.** Number density ( $\text{cm}^{-3}$ ) for gas-phase (left) and ice-phase (right)  $\text{CH}_3\text{OH}$  (left) at 1 (top), 2 (middle), and 5 (bottom) Myr as a function of disk radius,  $r$  and height divided by the radius,  $z/r$ . The contours in the top-left panel show the gas temperature at 40, 50, 70, and 150 K. The contours in the top-right panel show the strength of the UV radiation field in the disk at 0.01, 1, and 100 times  $G_0$ , where  $G_0 = 1.6 \times 10^{-3} \text{ erg cm}^{-2} \text{ s}^{-1}$  is the strength of the interstellar radiation field.





**Figure 16.** Number density ( $\text{cm}^{-3}$ ) for gas-phase (left) and ice-phase (right)  $\text{H}_2\text{CO}$  (left) at 1 (top), 2 (middle), and 5 (bottom) Myr as a function of disk radius,  $r$  and height divided by the radius,  $z/r$ . The contours in the top-left panel show the gas temperature at 40, 50, 70, and 150 K. The contours in the top-right panel show the strength of the UV radiation field in the disk at 0.01, 1, and 100 times  $G_0$ , where  $G_0 = 1.6 \times 10^{-3} \text{ erg cm}^{-2} \text{ s}^{-1}$  is the strength of the interstellar radiation field.

## ORCID iDs

Lucy Evans  <https://orcid.org/0009-0006-1929-3896>  
 Alice S. Booth  <https://orcid.org/0000-0003-2014-2121>  
 Catherine Walsh  <https://orcid.org/0000-0001-6078-786X>  
 John D. Ilee  <https://orcid.org/0000-0003-1008-1142>  
 Luke Keyte  <https://orcid.org/0000-0001-5849-577X>  
 Charles J. Law  <https://orcid.org/0000-0003-1413-1776>  
 Margot Leemker  <https://orcid.org/0000-0003-3674-7512>  
 Shota Notsu  <https://orcid.org/0000-0003-2493-912X>  
 Karin Öberg  <https://orcid.org/0000-0001-8798-1347>  
 Milou Temmink  <https://orcid.org/0000-0002-7935-7445>  
 Nienke van der Marel  <https://orcid.org/0000-0003-2458-9756>

## References

- ALMA Partnership, Brogan, C. L., Pérez, L. M., et al. 2015, *ApJL*, **808**, L3  
 Belloche, A., Maury, A. J., Maret, S., et al. 2020, *A&A*, **635**, A198  
 Bertin, M., Romanzin, C., Doronin, M., et al. 2016, *ApJL*, **817**, L12  
 Bianchi, E., López-Sepulcre, A., Ceccarelli, C., et al. 2022, *ApJL*, **928**, L3  
 Bockelée-Morvan, D., & Biver, N. 2017, *RSPTA*, **375**, 20160252  
 Booth, A. S., Ilee, J. D., Walsh, C., et al. 2023a, *A&A*, **669**, A53  
 Booth, A. S., Law, C. J., Temmink, M., Leemker, M., & Macias, E. 2023b, *A&A*, **678**, A146  
 Booth, A. S., Leemker, M., van Dishoeck, E. F., et al. 2024a, *AJ*, **167**, 164  
 Booth, A. S., Temmink, M., van Dishoeck, E. F., et al. 2024b, *AJ*, **167**, 165  
 Booth, A. S., Walsh, C., Kama, M., et al. 2018, *A&A*, **611**, A16  
 Booth, A. S., Walsh, C., Terwisscha van Scheltinga, J., et al. 2021, *NatAs*, **5**, 684  
 Bouvier, M., Ceccarelli, C., López-Sepulcre, A., et al. 2022, *ApJ*, **929**, 10  
 Briggs, D. S. 1995, PhD thesis, New Mexico Inst. Mining and Technology  
 Brittain, S. D., Carr, J. S., Najita, J. R., Quanz, S. P., & Meyer, M. R. 2014, *ApJ*, **791**, 136  
 Brown, W. A., & Bolina, A. S. 2007, *MNRAS*, **374**, 1006  
 Brunken, N. G. C., Booth, A. S., Leemker, M., et al. 2022, *A&A*, **659**, A29  
 Carney, M. T., Hogerheijde, M. R., Guzmán, V. V., et al. 2019, *A&A*, **623**, A124  
 Carney, M. T., Hogerheijde, M. R., Loomis, R. A., et al. 2017, *A&A*, **605**, A21  
 CASA Team, Bean, B., Bhatnagar, S., et al. 2022, *PASP*, **134**, 114501  
 Casassus, S., van der Plas, G. M., Perez, S., et al. 2013, *Natur*, **493**, 191  
 Ceccarelli, C., Codella, C., Balucani, N., et al. 2023, in ASP Conf. Ser. 534, *Protostars and Planets VII*, ed. S. Inutsuka et al. (San Francisco, CA: ASP), 379  
 Chen, Y. J., Ciaravella, A., Muñoz Caro, G. M., et al. 2013, *ApJ*, **778**, 162  
 Chen, Y., Rocha, W. R. M., van Dishoeck, E. F., et al. 2024, *A&A*, **690**, A205  
 Chuang, K. J., Fedoseev, G., Ioppolo, S., van Dishoeck, E. F., & Linnartz, H. 2016, *MNRAS*, **455**, 1702  
 Chuang, K. J., Fedoseev, G., Qasim, D., et al. 2017, *MNRAS*, **467**, 2552  
 Collings, M. P., Anderson, M. A., Chen, R., et al. 2004, *MNRAS*, **354**, 1133  
 Cruz-Díaz, G. A., Martín-Doménech, R., Muñoz Caro, G. M., & Chen, Y. J. 2016, *A&A*, **592**, A68  
 Cuppen, H. M., Walsh, C., Lamberts, T., et al. 2017, *SSRv*, **212**, 1  
 Czekala, I., Loomis, R. A., Teague, R., et al. 2021, *ApJS*, **257**, 2  
 Drozdovskaya, M. N., Walsh, C., Visser, R., Harsono, D., & van Dishoeck, E. F. 2014, *MNRAS*, **445**, 913  
 Drozdovskaya, M. N., Walsh, C., Visser, R., Harsono, D., & van Dishoeck, E. F. 2015, *MNRAS*, **451**, 3836  
 Dutrey, A., Guilloteau, S., & Guelin, M. 1997, *A&A*, **317**, L55  
 Endres, C. P., Schlemmer, S., Schilke, P., Stutzki, J., & Müller, H. S. 2016, *JMoSp*, **327**, 95  
 Evans, L., Vastel, C., Fontani, F., et al. 2023, *A&A*, **678**, A160  
 Fairlamb, J. R., Oudmaijer, R. D., Mendigutía, I., Ilee, J. D., & van den Ancker, M. E. 2015, *MNRAS*, **453**, 976  
 Fedele, D., Bruderer, S., van Dishoeck, E. F., et al. 2013, *A&A*, **559**, A77  
 Fedele, D., Toci, C., Maud, L., & Lodato, G. 2021, *A&A*, **651**, A90  
 Fedoseev, G., Chuang, K. J., Ioppolo, S., et al. 2017, *ApJ*, **842**, 52  
 Fockenberg, C., & Preses, J. M. 2002, *JPCA*, **106**, 2924  
 Foreman-Mackey, D., Hogg, D. W., Lang, D., & Goodman, J. 2013, *PASP*, **125**, 306  
 Fuchs, G. W., Cuppen, H. M., Ioppolo, S., et al. 2009, *A&A*, **505**, 629  
 Garrod, R., Park, I. H., Caselli, P., & Herbst, E. 2006, *FaDi*, **133**, 51  
 Garrod, R. T., & Pauly, T. 2011, *ApJ*, **735**, 15  
 Garrod, R. T., Widicus Weaver, S. L., & Herbst, S. L. 2008, *ApJ*, **682**, 283  
 Garufi, A., Podio, L., Codella, C., et al. 2020, *A&A*, **636**, A65  
 Garufi, A., Podio, L., Codella, C., et al. 2021, *A&A*, **645**, A145  
 Garufi, A., Podio, L., Codella, C., et al. 2022, *A&A*, **658**, A104  
 Geppert, W. D., Hamberg, M., Thomas, R. D., et al. 2006, *FaDi*, **133**, 177  
 Goldsmith, P. F., & Langer, W. D. 1999, *ApJ*, **517**, 209  
 Graninger, D. M., Wilkins, O. H., & Öberg, K. I. 2016, *ApJ*, **819**, 140  
 Guilloteau, S., Di Folco, E., Dutrey, A., et al. 2013, *A&A*, **549**, A92  
 Guzmán, V. V., Bergner, J. B., Law, C. J., et al. 2021, *ApJS*, **257**, 6  
 Guzmán, V. V., Goicoechea, J. R., Pety, J., et al. 2013, *A&A*, **560**, A73  
 Hasegawa, T. I., Herbst, E., & Leung, C. M. 1992, *ApJS*, **82**, 167  
 Herbst, E., & van Dishoeck, E. F. 2009, *ARA&A*, **47**, 427  
 Hernández-Vera, C., Guzmán, V. V., Artur de la Villarmois, E., et al. 2024a, *ApJ*, **967**, 68  
 Hiraoka, K., Ohashi, N., Kihara, Y., et al. 1994, *CPL*, **229**, 408  
 Hsu, S.-Y., Liu, S.-Y., Liu, T., et al. 2020, *ApJ*, **898**, 107  
 Ilee, J. D., Walsh, C., Booth, A. S., et al. 2021, *ApJS*, **257**, 9  
 Jørgensen, J. K., Belloche, A., & Garrod, R. T. 2020, *ARA&A*, **58**, 727  
 Jorsater, S., & van Moorsel, G. A. 1995, *AJ*, **110**, 2037  
 Kama, M., Bruderer, S., van Dishoeck, E. F., et al. 2016, *A&A*, **592**, A83  
 Keyte, L., Kama, M., Booth, A. S., et al. 2023, *NatAs*, **7**, 684  
 Lee, C.-F., Codella, C., Ceccarelli, C., & López-Sepulcre, A. 2022, *ApJ*, **937**, 10  
 Lee, J.-E., Lee, S., Baek, G., et al. 2019, *NatAs*, **3**, 314  
 Leemker, M., Booth, A. S., van Dishoeck, E. F., et al. 2023, *A&A*, **673**, A7  
 Leemker, M., Booth, A. S., van Dishoeck, E. F., Wölfer, L., & Dent, B. 2024, *A&A*, **687**, A299  
 Ligterink, N. F. W., Kipfer, K. A., & Gavino, S. 2024, *A&A*, **687**, A224  
 Ligterink, N. F. W., & Minissale, M. 2023, *A&A*, **676**, A80  
 Lindegren, L., Lammers, U., Bastian, U., et al. 2016, *A&A*, **595**, A4  
 Lippi, M., Podio, L., Codella, C., et al. 2024, *ApJL*, **970**, L5  
 Loomis, R. A., Cleeves, L. I., Öberg, K. I., Guzman, V. V., & Andrews, S. M. 2015, *ApJL*, **809**, L25  
 Loomis, R. A., Cleeves, L. I., Öberg, K. I., et al. 2018, *ApJ*, **859**, 131  
 Loomis, R. A., Öberg, K. I., Andrews, S. M., et al. 2020, *ApJ*, **893**, 101  
 Manigand, S., Jørgensen, J. K., Calcutt, H., et al. 2020, *A&A*, **635**, A48  
 Martín-Doménech, R., Muñoz Caro, G. M., & Cruz-Díaz, G. A. 2016, *A&A*, **589**, A107  
 McClure, M. K., Rocha, W. R. M., Pontoppidan, K. M., et al. 2023, *NatAs*, **7**, 431  
 McElroy, D., Walsh, C., Markwick, A. J., et al. 2013, *A&A*, **550**, A36  
 Meinert, C., Myrgorodska, I., de Marcellus, P., et al. 2016, *Sci*, **352**, 208  
 Mercimek, S., Codella, C., Podio, L., et al. 2022, *A&A*, **659**, A67  
 Miettinen, O. 2016, *Ap&SS*, **361**, 248  
 Miley, J. M., Panić, O., Haworth, T. J., et al. 2019, *MNRAS*, **485**, 739  
 Minissale, M., Aikawa, Y., Bergin, E., et al. 2022, *ESC*, **6**, 597  
 Müller, H. S. P., & Lewen, F. 2017, *JMoSp*, **331**, 28  
 Müller, H. S. P., Thorwirth, S., Roth, D. A., & Winnewisser, G. 2001, *A&A*, **370**, L49  
 Müller, H. S., Schlder, F., Stutzki, J., & Winnewisser, G. 2005, *JMoSt*, **742**, 215  
 Noble, J. A., Theule, P., Mispelaer, F., et al. 2012, *A&A*, **543**, A5  
 Notsu, S., van Dishoeck, E. F., Walsh, C., Bosman, A. D., & Nomura, H. 2021, *A&A*, **650**, A180  
 Öberg, K. I., Garrod, R. T., van Dishoeck, E. F., & Linnartz, H. 2009, *A&A*, **504**, 891  
 Öberg, K. I., Linnartz, H., Visser, R., & van Dishoeck, E. F. 2009, *ApJ*, **693**, 1209  
 Öberg, K. I., Qi, C., Fogel, J. K. J., et al. 2011, *ApJ*, **734**, 98  
 Ospina-Zamudio, J., Lefloch, B., Ceccarelli, C., et al. 2018, *A&A*, **618**, A145  
 Pegues, J., Öberg, K. I., Bergner, J. B., et al. 2020, *ApJ*, **890**, 142  
 Penteado, E. M., Walsh, C., & Cuppen, H. M. 2017, *ApJ*, **844**, 71  
 Persson, M. V., Jørgensen, J. K., Müller, H. S. P., et al. 2018, *A&A*, **610**, A54  
 Pineda, J. E., Szulágyi, J., Quanz, S. P., et al. 2019, *ApJ*, **871**, 48  
 Pinilla, P., Birnstiel, T., & Walsh, C. 2015, *A&A*, **580**, A105  
 Pirovano, L. M., Fedele, D., van Dishoeck, E. F., et al. 2022, *A&A*, **665**, A45  
 Podio, L., Bacciotti, F., Fedele, D., et al. 2019, *A&A*, **623**, L6  
 Podio, L., Garufi, A., Codella, C., et al. 2020, *A&A*, **642**, L7  
 Puanova, A., Caselli, P., Feng, S., et al. 2018, *ApJ*, **855**, 112  
 Qi, C., D'Alessio, P., Öberg, K. I., et al. 2011, *ApJ*, **740**, 84  
 Quanz, S. P., Amara, A., Meyer, M. R., et al. 2013, *ApJL*, **766**, L1  
 Rabli, D., & Flower, D. R. 2010, *MNRAS*, **406**, 95  
 Rampinelli, L., Facchini, S., Leemker, M., et al. 2024, *A&A*, **689**, A65  
 Riaz, B., Thi, W. F., & Machida, M. N. 2023, *MNRAS*, **522**, 4934  
 Rocha, W. R. M., van Dishoeck, E. F., Ressler, M. E., et al. 2024, *A&A*, **683**, A124  
 Schöier, F. L., van der Tak, F. F. S., van Dishoeck, E. F., & Black, J. H. 2005, *A&A*, **432**, 369  
 Scibelli, S., & Shirley, Y. 2020, *ApJ*, **891**, 73

- Semenov, D., & Wiebe, D. 2011, [ApJS](#), **196**, 25
- Simons, M. A. J., Lamberts, T., & Cuppen, H. M. 2020, [A&A](#), **634**, A52
- Taquet, V., López-Sepulcre, A., Ceccarelli, C., et al. 2015, [ApJ](#), **804**, 81
- Teague, R. 2019, [JOSS](#), **4**, 1632
- Teague, R. 2020, `richteague/keplerian_mask`: Initial Release, v1.0, Zenodo, doi:[10.5281/zenodo.4321137](#)
- Temmink, M., Booth, A. S., van der Marel, N., & van Dishoeck, E. F. 2023, [A&A](#), **675**, A131
- Temmink, M., Booth, A. S., Leemker, M., et al. 2025, [A&A](#), **693**, A101
- Terwisscha van Scheltinga, J., Hogerheijde, M. R., Cleeves, L. I., et al. 2021, [ApJ](#), **906**, 111
- Thi, W. F., van Zadelhoff, G. J., & van Dishoeck, G. J. 2004, [A&A](#), **425**, 955
- Tielens, A. G. G. M., & Hagen, W. 1982, [A&A](#), **114**, 245
- van der Marel, N. 2023, [EPJP](#), **138**, 225
- van der Marel, N., Booth, A. S., Leemker, M., van Dishoeck, E. F., & Ohashi, S. 2021, [A&A](#), **651**, L5
- van't Hoff, M. L. R., Harsono, D., Tobin, J. J., et al. 2020, [ApJ](#), **901**, 166
- van't Hoff, M. L. R., Tobin, J. J., Trapman, L., et al. 2018, [ApJL](#), **864**, L23
- van't Hoff, M. L. R., Walsh, C., Kama, M., Facchini, S., & van Dishoeck, E. F. 2017, [A&A](#), **599**, A101
- Vastel, C., Alves, F., Ceccarelli, C., et al. 2022, [A&A](#), **664**, A171
- Walsh, C., Daley, C., Facchini, S., & Juhász, A. 2017, [A&A](#), **607**, A114
- Walsh, C., Juhász, A., Pinilla, P., et al. 2014, [ApJL](#), **791**, L6
- Walsh, C., Loomis, R. A., Öberg, K. I., et al. 2016, [ApJL](#), **823**, L10
- Walsh, C., Millar, T. J., & Nomura, H. 2010, [ApJ](#), **722**, 1607
- Walsh, C., Millar, T. J., & Nomura, H. 2013, [ApJL](#), **766**, L23
- Walsh, C., Nomura, H., Millar, T. J., & Aikawa, Y. 2012, [ApJ](#), **747**, 114
- Walsh, C., Nomura, H., & van Dishoeck, E. 2015, [A&A](#), **582**, A88
- Walsh, C., Vissapragada, S., & McGee, H. 2018, in *IAU Symp. 332, Astrochemistry VII: Through the Cosmos from Galaxies to Planets*, ed. M. Cunningham, T. Millar, & Y. Aikawa (Cambridge: Cambridge Univ. Press), 395
- Watanabe, N., & Kouchi, A. 2002, [ApJL](#), **571**, L173
- Wichittanakom, C., Oudmaijer, R. D., Fairlamb, J. R., et al. 2020, [MNRAS](#), **493**, 234
- Wiesenfeld, L., & Faure, A. 2013, [MNRAS](#), **432**, 2573
- Wölfer, L., Izquierdo, A. F., Booth, A. S., et al. 2024, [A&A](#), submitted
- Wright, C. M., Maddison, S. T., Wilner, D. J., et al. 2015, [MNRAS](#), **453**, 414
- Xu, L.-H., Fisher, J., Lees, R. M., et al. 2008, [JMoSp](#), **251**, 305
- Yamato, Y., Aikawa, Y., Guzmán, V. V., et al. 2024, [ApJ](#), **974**, 83
- Yang, Y.-L., Sakai, N., Zhang, Y., et al. 2021, [ApJ](#), **910**, 20
- Zhang, K., Bergin, E. A., Schwarz, K., Krijt, S., & Ciesla, F. 2019, [ApJ](#), **883**, 98
- Zhang, K., Booth, A. S., Law, C. J., et al. 2021, [ApJS](#), **257**, 5